The Thesis Committee for Matthew Louis Wisher
Certifies that this is the approved version of the following thesis (or report):

MegaGauss: A Portable 40T Magnetic Field Generator

APPROVED BY
SUPERVISING COMMITTEE:

Supervisors:

Gary Hallock

Roger Bengtson

MegaGauss: A Portable 40T Magnetic Field Generator

by

Matthew Louis Wisher, B.S.

Thesis

Presented to the Faculty of the Graduate School of

The University of Texas at Austin

in Partial Fulfillment

of the Requirements

for the Degree of

Master of Science in Engineering

The University of Texas at Austin

May 2011

Dedication

To my parents, who homeschooled me from my first day of kindergarten through my last day of high school, helped me through college, and continue to encourage me through my graduate career, all despite my numerous faults and occasional ungratefulness, I dedicate this work.

Acknowledgements

I would like to acknowledge my advisers, Dr. Gary Hallock of the electrical engineering department, and Dr. Roger Bengtson of the physics department. Both have been tremendously helpful and supportive in their comments during the writing of this thesis, and have made the process more than manageable.

Several scientists at Sandia National Laboratories have been tremendously helpful during the course of the experiments outlined in this thesis. Two that stand out are Dr. Kenneth Struve and Mr. Brian Stoltzfus. Both of them have contributed extensively to my understanding of pulsed power, and the instrumentation and special considerations that accompany operating experiments in that regime of physics.

I would like to thank Dr. Hernan Quevedo for his patient tutoring in all manner of experimental techniques, from signal acquisition to optics. My fellow student in this project, Mr. Sean Lewis, has also been a source of rewarding and enjoyable conversations through the course of these experiments.

Lastly, I would like to appreciate my family for their steadfast encouragement of my academic pursuits, without which this journey would be very difficult indeed.

May 6, 2011

Abstract

MegaGauss: A Portable 40T Magnetic Field Generator

Matthew Louis Wisher, MSE

The University of Texas at Austin, 2011

Supervisors: Gary Hallock and Roger Bengtson

Fusion neutrons from high energy density plasmas generated by pulsed laser irradiation of nanoscale atomic clusters have been explored in recent experiments at the University of Texas at Austin. A sufficiently strong (~200 T) magnetic field is expected to produce a magnetized, high temperature (10 keV) plasma with beta ≈ 1. Such a field along the laser axis may confine the plasma's radial expansion, thus increasing fusion yield.

As part of a multi-stage project to implement this experiment, a scaled (~40 T, ~500 KA) version of the final 200 T, 2.2 MA pulsed power device has been designed and built by Sandia National Laboratories and is now at UT-Austin. This apparatus, named MegaGauss, is meant to serve as a preparation tool for the 200 T system; as such, its

current pulse was recorded for analysis, and is compared to a theoretical model to verify its response parameters (e.g. peak current, time to peak).

Techniques and results of this comparison are discussed, followed by explanations of basic construction of the 40 T device and current sensing instrumentation. Discussion of MegaGauss is completed with a survey of notable failure modes, and a description of the often severe effects the miniature field-generating Helmholtz coil experiences due to the current pulse and magnetic field.

Finally, a novel data archive scheme, structured around the familiar MDSplus archive system, is implemented in Labview and integrated into the main pulsed power control program. Specifically, methods for linking MDSplus's robust functionality with Labview's intuitive development environment are realized by means of a specialized software bridge between the two. These methods are used in software that allows MDSplus archives to be written and read exclusively through Labview.

Table of Contents

List of Tables

List of Figures

Chapter 1: Current Response of MegaGauss

1.1. MEGAGAUSS OVERVIEW

Recent experiments with high intensity laser pulses incident upon nanoscale atomic clusters have revealed a unique method of providing a target into which laser energy may be coupled, creating a high energy density (HED) plasma (1). Due to the mechanics of the plasma's formation, appropriately engineered clusters have been found to be suitable fuel for nuclear fusion reactions (specifically, $D + D \rightarrow He + n$). In these experiments, the plasma filament formed in the laser's focal region is free to expand in every direction at the thermal velocity ($v_{th} = \sqrt{kT/m}$). To confine this expansion radially, scientists at Sandia National Laboratories have designed and built a pulsed power device to impose an intense (~200 T) magnetic field into the plasma. (2) By restricting the plasma's expansion to one dimension (axial), this confinement scheme is expected to provide more opportunity for fusion reactions.

As a testing and proof-of-concept platform, a scaled down system has been built and currently resides at the University of Texas at Austin physics department, and is capable of generating approximately 20% of the energy output of the 200 T system. Initial testing has been performed with this apparatus, henceforth referred to as MegaGauss, to facilitate understanding of the instrumentation and architecture of the 200 T device, and to gain experience operating within the pulsed power regime. Much of the technology is directly relatable to the ring architecture (Fig 1.1) used in contemporary pulsed power facilities. For this 20% system, only two current sources (capacitor, switch, pulse conditioning, and transmission line) are used, but the architecture allows for more if desired; in the 200 T case, up to ten sources will be available.

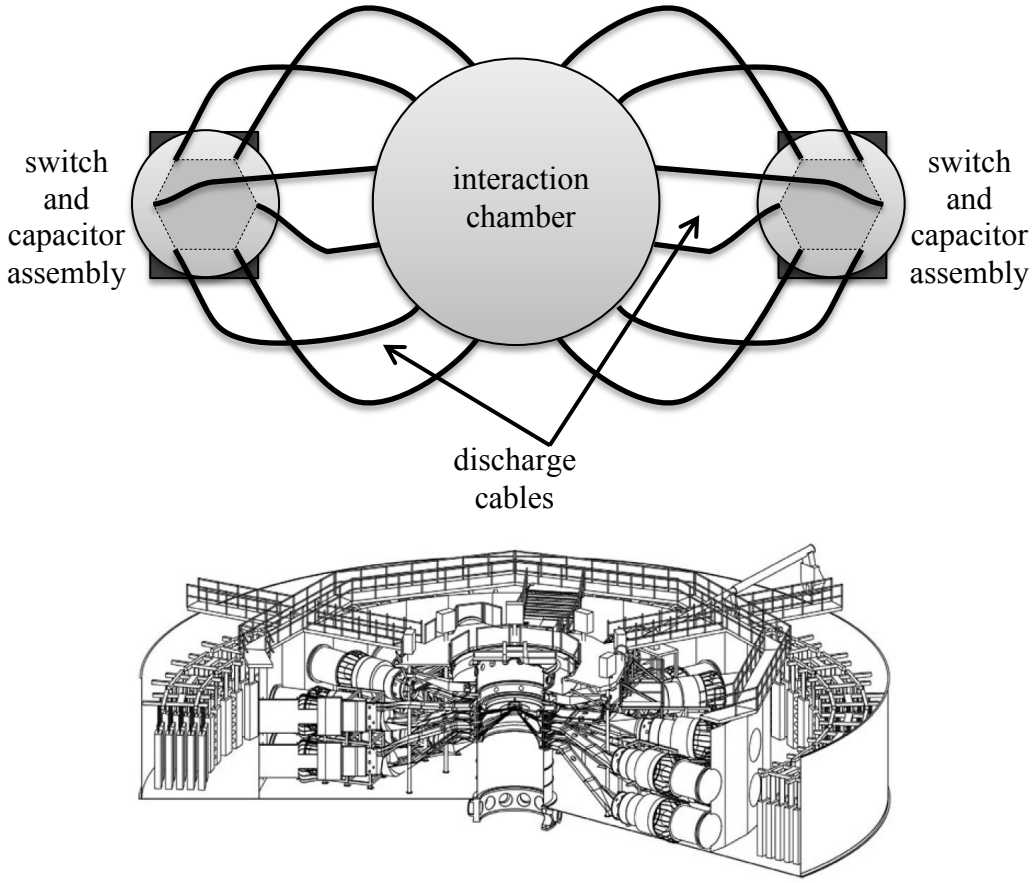

Figure 1.1: Top: overhead schematic diagram of MegaGauss driver assembly. External charging and triggering connections not pictured. Bottom: cutaway image of Z Machine at Sandia National Laboratories. (3) Note the ring topology.

Over three hundred shots have been fired in MegaGauss so far, and these shots have provided a valuable collection of data that will guide the implementation of the larger system. A theoretical model, detailed shortly hereafter (§1.3.1), indicates that at 100% energy (100 KV per capacitor), MegaGauss should be capable of attaining a peak current of 454 KA within 1.6 μs, with the current diminishing linearly with energy (e.g. 50% yields 227 KA). Such a current will produce 42 T in an appropriately shaped field-generating coil (§5.3.3). As its primary purpose, MegaGauss, as a scaled version of the

200 T system, is configured to verify this theoretical model. Before examining the overall construction of MegaGauss, we will compare the theoretical model with experimental data and show MegaGauss falls within an acceptable range of performance. Secondary experiment results will be detailed later.

At its core, the MegaGauss system may be thought of as a specialized series RLC circuit, in which the specialization comes about due to the very low (~100 nH) circuit inductance. This enables the fast rise time required to allow MegaGauss to reach the pulsed power regime. First, we will examine the differential equation governing a series RLC circuit and how the various constants in the equation may be extracted from a plot of the circuit response. We will then proceed to compute an expected waveform, based on estimates for the circuit resistance, inductance, and capacitance. Also, the parameters of the differential equation's response will be expressed in terms of the circuit's component's values. Finally, experimental data will be compared to the expected circuit response. Also, the decay constant, the resonant frequency, and peak amplitude will be used to obtain the circuit element values experimentally, and will be compared with the theoretical estimates.

1.2. RLC GOVERNING EQUATION

In the case of MegaGauss, the circuit response is underdamped. This allows for maximum amplitude in the response, but also subjects the capacitors to reverse voltage. One of the design parameters governing MegaGauss's design is the maximum reverse voltage the capacitors will be required to withstand. (2) To facilitate a formal comparison of the mathematical model of the circuit with the shot data, we will begin this section by examining the underdamped solution to the differential equation for the current in a series RLC circuit (Fig. 1.2). (4)

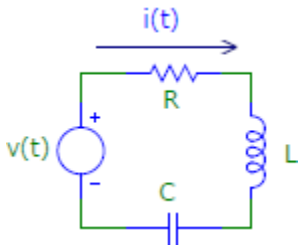

Figure 1.2: Archetype for a series RLC circuit.

The series RLC current response can be modeled by the following differential equation:

$$Ri(t) + L\frac{di}{dt} + \frac{1}{C}\int_{-\infty}^{\tau=t} i(\tau)d\tau = v(t), \tag{1.1}$$

where in this case, $v(t) \equiv 0$, i.e. no forcing function; the circuit is energized by the capacitor discharge at $t = 0$. The solution is:

$$i(t) = B_1 e^{-\alpha t}\cos(\omega_d\, t) + B_2 e^{-\alpha t}\sin(\omega_d\, t), \tag{1.2}$$

$$\omega_d = \sqrt{\omega_0^2 - \alpha^2} = \omega_0\sqrt{1-\zeta^2}, \tag{1.3}$$

where values for constants B_1 and B_2 are computed from boundary conditions. Since this RLC system is energized by a capacitor discharge occurring at $t = 0$, a boundary condition exists on the initial value for current, namely $i(0) = 0$. Therefore, the cosine term in the general solution may be immediately discarded, leaving

$$i(t) = I_0 e^{-\alpha t}\sin(\omega_d\, t), \tag{1.4}$$

leading to the conclusion that the underdamped response takes the form of a damped sine wave (e.g. Fig. 1.3).

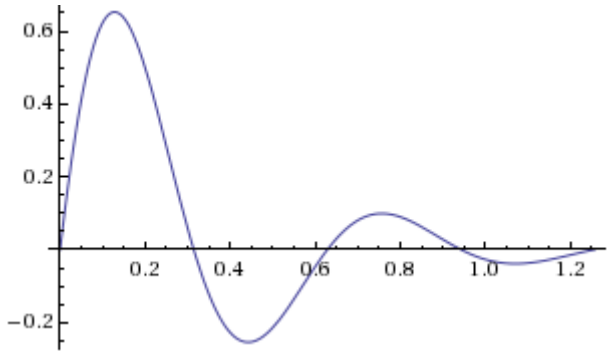

Figure 1.3: Example of underdamped sinusoid. $y(x) = e^{-3x}\sin(10x)\,, x = [0, \pi/2.5]$.

In general, it is possible to take two data points from such a plot and determine several parameters of the RLC response. First, given two consecutive zeros at times t_1 and t_2, the characteristic frequency has the simple solution:

$$\omega_d = \pi/(t_2 - t_1). \tag{1.5}$$

Once this frequency is obtained, it can be entered into the general solution of the RLC response and used with any two points, designated as those at times t_3 and t_4, to solve for the decay constant α and amplitude I_0:

$$i(t_3) = I_0 e^{-\alpha t_3}\sin(\omega_d\, t_3), \tag{1.6}$$

$$i(t_4) = I_0 e^{-\alpha t_4}\sin(\omega_d\, t_4). \tag{1.7}$$

Solving simultaneously gives:

$$\alpha = \frac{1}{t_4 - t_3} ln\left[\frac{I(t_3)\sin(\omega_d t_4)}{I(t_4)\sin(\omega_d t_3)}\right], \tag{1.8}$$

$$I_0 = \frac{I(t_3)}{\sin(\omega_d t_3)}\left[\frac{I(t_3)\sin(\omega_d t_4)}{I(t_4)\sin(\omega_d t_3)}\right]^{\frac{t_3}{t_4 - t_3}}. \tag{1.9}$$

All essential parameters of the response equation have now been computed. The relationship between the RLC circuit values and the response parameters are derived from the differential equation governing the response, and are shown below for a series RLC circuit:

$$\alpha = \frac{R}{2L}, \qquad \omega_0 = \frac{1}{\sqrt{LC}} \tag{1.10, 11}$$

In the case of the MegaGauss circuit, the large capacitance of the storage capacitors ensure that parasitic capacitance (from cabling, for example), is negligible. Thus, it can be said that $C \approx 3.1\,\mu F$ per channel. Now, only two variables must be calculated, greatly simplifying the process of extracting the RLC values from the recorded response of the circuit. Also, total inductance will be on the order of a few hundred nanohenries, and resistance will be on the order of a hundred milliohms. Thus, it may also be expected that $\zeta^2 = R^2C/(4L) \sim 10^{-2}$, implying $\omega_d = \omega_0\sqrt{1-\zeta^2} \approx \omega_0$. This will be illustrated when an approximate model for the system is computed.

1.3. THEORY VS. EXPERIMENT

1.3.1. Theoretical Results

A simplified model for the circuit (Fig. 1.4) will be used to compute the expected response of the two-capacitor MegaGauss configuration. See Appendix A for a complete circuit diagram and a list of circuit element values. Most elements are combined in parallel, except for the chamber transmission line and the load. The circuit is simply the same RLC circuit repeated twice, feeding into the same transmission line and load. By taking the elements of each channel in parallel, the circuit simplifies to the archetype RLC circuit (Fig. 1.1), where $R = R_1 \backslash\backslash R_2$, $L = L_1 \backslash\backslash L_2$ and $C = C_1 + C_2$.

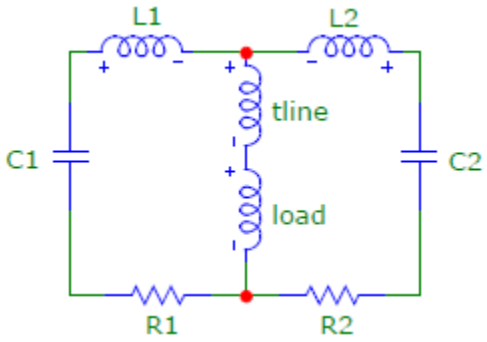

Figure 1.4: Simplified model of MegaGauss two-channel pulsed power system.

Estimated values (Table 1.1) for each component in the simplified model are computed by appropriately combining the elements of the more extensive circuit found in Appendix A. These values are used to compute component values for the RLC archetype (Fig. 1.2), upon which the differential equation model is based.

Figure 1.4	Figure 1.2
$R_1 = 100\ m\Omega$	$R = 50\ m\Omega$
$R_2 = 100\ m\Omega$	$L = 203\ nH$
$L_1 = 359\ nH$	$C = 6.22\ \mu F$
$L_2 = 359\ nH$	
$C_1 = 3.11\ \mu F$	
$C_2 = 3.11\ \mu F$	
$L_{tline} = 5.2\ nH$	
$L_{load} = 18\ nH$	

Table 1.1: Sums of estimated (5) component values for the simplified circuit models of MegaGauss. Values for individual components may be found in Appendix. A.

Based on these values, we now solve for the response parameters:

$$\alpha = \frac{R}{2L} = 123 \times 10^3\ s^{-1}, \tag{1.12}$$

$$\omega_0 = \frac{1}{\sqrt{LC}} = 892 \times 10^3\ rad/s = 142\ KHz \tag{1.13}$$

$$\omega_d = \sqrt{\omega_0^2 - \alpha^2} = 884 \times 10^3\ \ rad/s = 141\ KHz, \tag{1.14}$$

$$I_0[Amps] = \frac{V_0}{|Z|} \approx \frac{V_0}{|iL\omega_d|} = 5.58 \cdot V_0[Volts] \tag{1.15}$$

As alluded to earlier, and now confirmed by Eqns. 1.13-14, $\omega_d \approx \omega_0$. We are now able to compute a model response, given an initial capacitor voltage. Since most shots were fired at 50% charge (50 KV), we choose $V_0 = 50\ KV$. Thus, the response predicted by the model is:

$$i(t) = (279 \times 10^3)e^{-(123\times10^3)t} \sin[(884 \times 10^3)t], \tag{1.16}$$

whose time response is pictured in Figure 1.5.

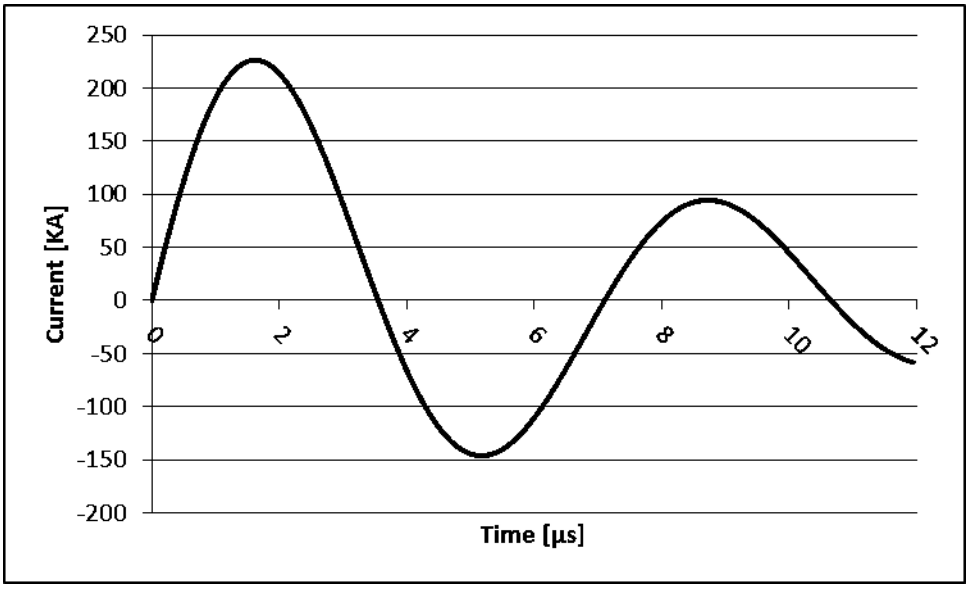

Figure 1.5: Visualization of theoretical response based on Eqn. 1.16.

Additional response statistics are now easily visualized, and are displayed alongside those already computed:

- Peak current = 226 KA
- Time to peak = 1.62 μs
- Characteristic frequency = 141 KHz
- Decay time constant = 123×10^3 s^{-1}
- Maximum reverse voltage ≈ $(-146 \times 10^3$ A) / (5.58 A / V) = -26.2 KV, 52.4% of initial charge voltage.

These theoretical values computed from estimated component characteristics will now be compared with shot data acquired during the initial testing phase of MegaGauss.

1.3.2. Measured Results

Now that the theoretical response of a series RLC circuit operating in the pulsed power regime has been explored, we will work in the opposite direction by measuring plots from shot data and analyzing them, with the purpose of extracting the response parameters and circuit component values. The shots in use for this procedure will be shots that were fired shortly after both switch B-dot current sensors were calibrated. These will be the earliest calibrated measurements of the MegaGauss system's response.

The total current in MegaGauss can be computed two ways. First, the current sourced from each switch assembly can be added, and by Kirchhoff's current law, this can be said to be the current into the system. This is prone to error, however, since a short somewhere within the interaction chamber would likely not have a noticeable effect on the system response. Thus, the second method of current measurement uses a third B-dot to sense the magnetic field produced by current flow through the electrical load, typically a copper Helmholtz coil (Figs. 5.2-3, Appx. A.3)

This second method of using an extra B-dot is far more robust, as it indicates the amount of current that the load actually receives. Also, this is the best diagnostic for detecting a short during the pulse's evolution; if the load's current suddenly jumps from the expected damped sinusoidal behavior predicted by the addition of the switch currents (Fig 4.1), the occurrence and time of the short becomes apparent. This third B-dot is typically calibrated by adding the known currents from the two switch assemblies, and adjusting the load B-dot's scaling factor to match their sum. Of course, it is preferable to have a calibrated B-dot based off the signal from a known magnetic field. Unfortunately, lack of symmetry in the load prevents a concrete understanding of the field distribution, complicating the calculation of the current from the measurement of the field. This difficulty is compounded by the frequent movement of the B-dot during load adjustment, requiring frequent measurement of coil position, assuming a fringing field pattern is available. Thus, the B-dot is calibrated under the assumption that a successful shot has all the current from the switch assemblies reaching the load.

Now that the general data collection scheme has been explained, some ideal data shots will be presented, analyzed, and compared with the theoretical results. Discussion of several failed shots to illustrate the diagnostic facility of the third (load) B-dot detection scheme is presented in Chapter 4.

Current measurements acquired from shots 86 and 87 are pictured in Figure 1.6. Both shots were fired under the same conditions, shortly after B-dot calibration was complete. Both shots resulted in smooth current readings (i.e. no abrupt changes in the plots due to shorting, etc.), making them ideal for analyzing the RLC characteristics of the system. For each plot, the relevant data points will be obtained, and the formulae

derived in the last section will be utilized to compute the apparent resistance, inductance, and capacitance of the circuit.

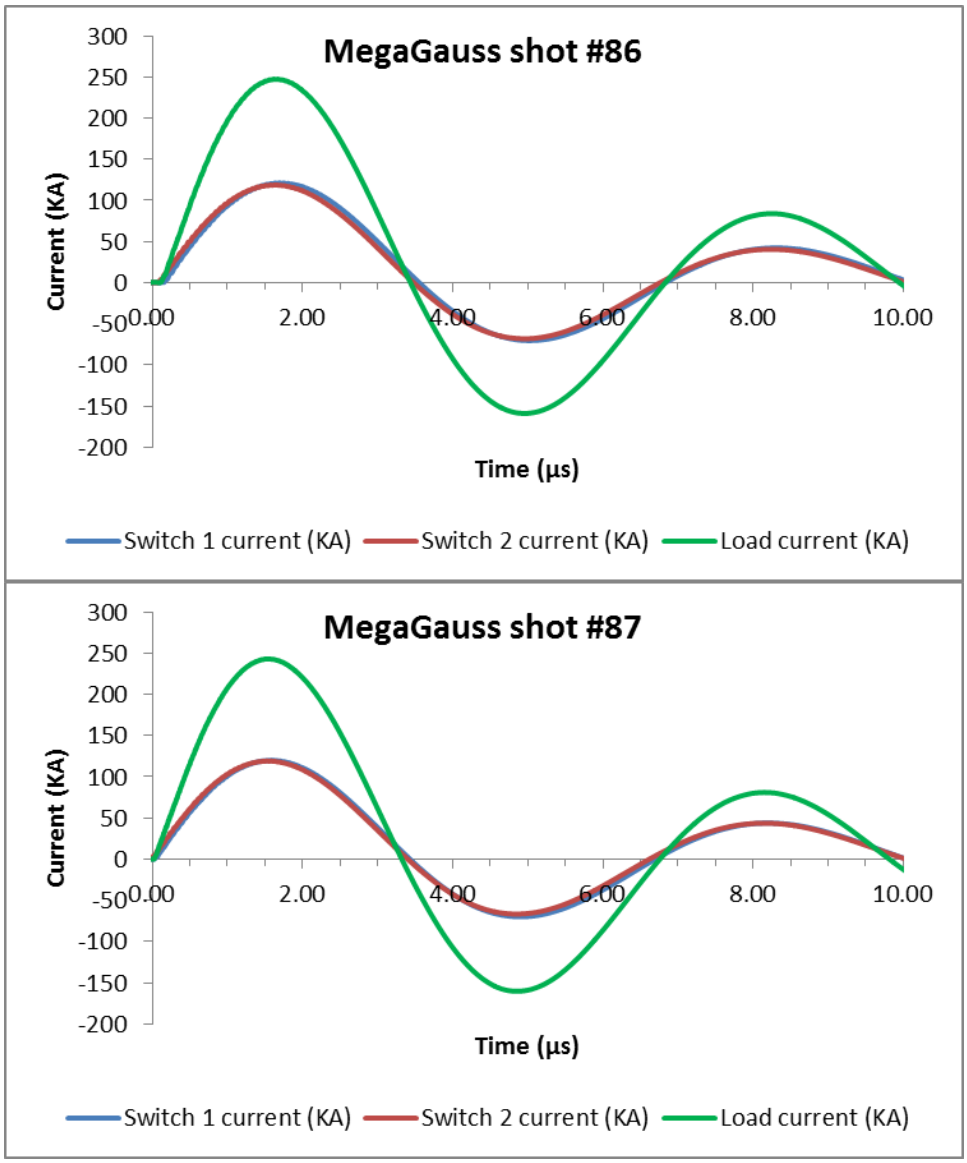

Figure 1.6: Current data obtained from MegaGauss shots 86 and 87.

	Shot #86	Shot #87	Mean
First zero time (t_1) [μs]	0.00	0.00	0.00
Second zero time (t_1) [μs]	3.36	3.32	3.34
$\omega_d(f_d)$ [rad/s (KHz)]	9.36×10^5 (149)	9.46×10^5 (151)	9.41×10^5 (150)
First measurement time (t_3) [μs]	2.00	5.00	N/A
Second measurement time (t_4) [μs]	2.00	5.00	N/A
$I(t_3) = I_3$ [KA]	234	228	231
$I(t_4) = I_4$ [KA]	-159	-160	-160
α [s^{-1}]	1.44×10^5	1.35×10^5	1.40×10^5
I_0 [KA]	327	315	321

Table 1.2: Raw and derived measurements from MegaGauss shots 86 and 87.

In calculating the circuit component values experimentally, we assume the large capacitance of the two storage capacitors dominate all other capacitances in the system, allowing an easier calculation of ω_0. Also, based on the values above, the relation

$$\omega_d = \sqrt{\omega_0^2 - \alpha^2} \tag{1.17}$$

implies $\omega_0 \gg \alpha$, thus we can say

$$\omega_d \approx \omega_0 = 1/\sqrt{L \cdot 6.22\ \mu F} \Rightarrow L \approx (\omega_d^2 \cdot 6.22\ \mu F)^{-1} \tag{1.18}$$

$$R = 2\alpha L \approx 2\alpha \cdot (\omega_d^2 \cdot 6.22\ \mu F)^{-1} \tag{1.19}$$

With these relations, and the values from the two data shots under review (Table 1.2), we find:

	Shot #86	Shot #87	Mean	Theoretical	% difference
R $[m\Omega]$	52.9	48.7	50.8	50.0	1.6%
L $[nH]$	184	180	182	203	10.3%
C $[\mu F]$	6.22	6.22	6.22	6.22	N/A

Table 1.3: Circuit component values computed from current response in MegaGauss shots 86 and 87 are compared with theoretical predictions.

These experimental results show satisfactory agreement with the expected theoretical values, and suggest that the MegaGauss system is functioning as it was designed. The near 10% inductance error is likely due to the number of component inductance estimates, but the actual and theoretical values are certainly well within the same order of magnitude. Over the course of over three hundred shots, the output has maintained the same characteristics, except for incidents that preclude normal operation (e.g. undesirable electrical breakdown).

Chapter 2: Experiment Apparatus

2.1. Interaction Chamber

In the center of MegaGauss's ring architecture is an interaction chamber. This chamber is meant to be reusable over the course of hundreds of shots with minimal refurbishing. It is also designed to be a high vacuum vessel, as the chamber must have the ability to accept high intensity laser pulses, whose efficiency relies in part upon propagation through vacuum. Several ports are provided at various positions on the chamber to allow for diagnostics and vacuum equipment, in addition to the primary laser pulse port.

Electrically, the chamber houses a tri-plate transmission line, where each plate is initially flat and circular on the perimeter, transitions into a conical shape, then flattens once more just before the cone comes to a point. Together, these three plates form the transmission line stack, with the two outer plates being the cathode, and the middle plate the anode. At the flat-top center of the stack is the anode, and surrounding this anode interface is a flat, narrow ring connected to the cathode. Finally, the space between these two contacts is bridged by the electrical load, which may take on different forms depending on the experiment requirements. Several smooth openings have been shaped into the plates to allow for contact between the two cathode plates, and to facilitate airflow between and below the conical plates.

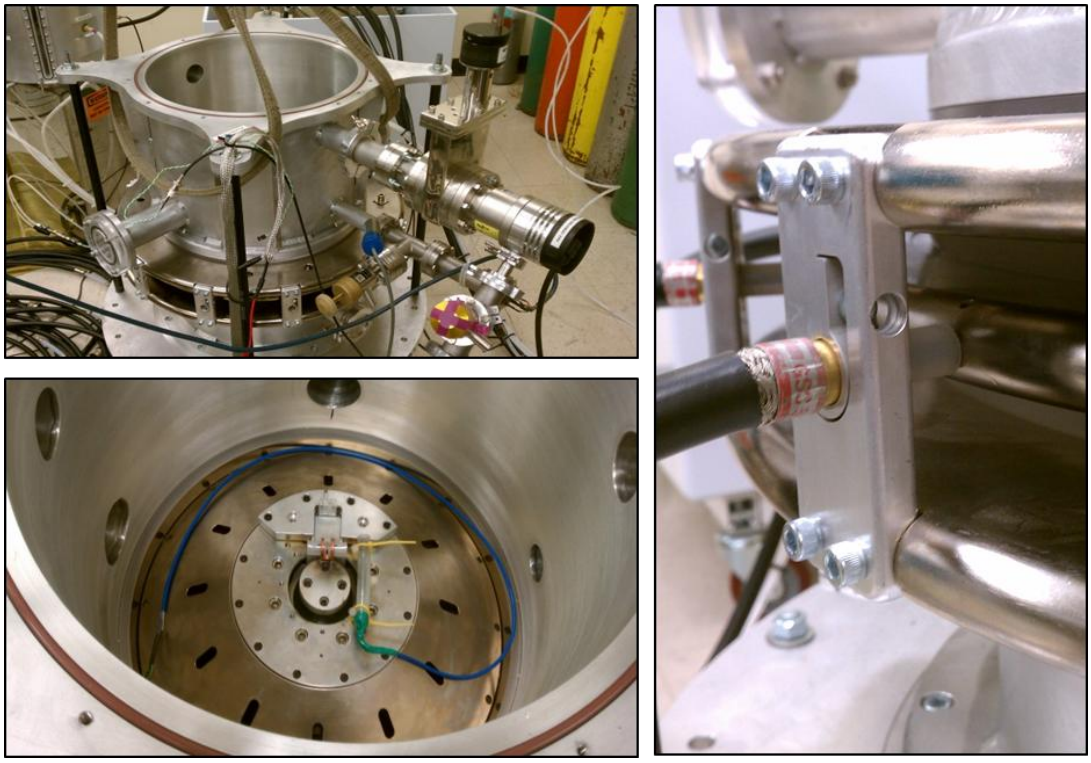

Figure 2.1: Interaction chamber. Top left: entire chamber with lid removed, turbomolecular pump attached on right. Bottom left: interior of chamber, conical tri-plate transmission line, coil, coil clamp, and load B-dot visible. Right: detail of cable insertion into transmission line perimeter.

Feedthroughs for the pulsed power are implemented by attaching coaxial cables from the current source to the perimeter of the plates (Fig. 2.1). To maintain the vacuum barrier of the chamber, and provide electrical insulation between the transmission line plates, two trapezoidal dielectric rings with O-ring seals on either side form the portion of the chamber wall where the transmission line enters the chamber. These shaped rings prevent electronic cascades between the transmission line plates (§3.1). Two thin, flat insulating rings are also placed between the two cathode plates and the chamber wall, but these are only meant to provide electrical isolation, not prevent electronic cascades.

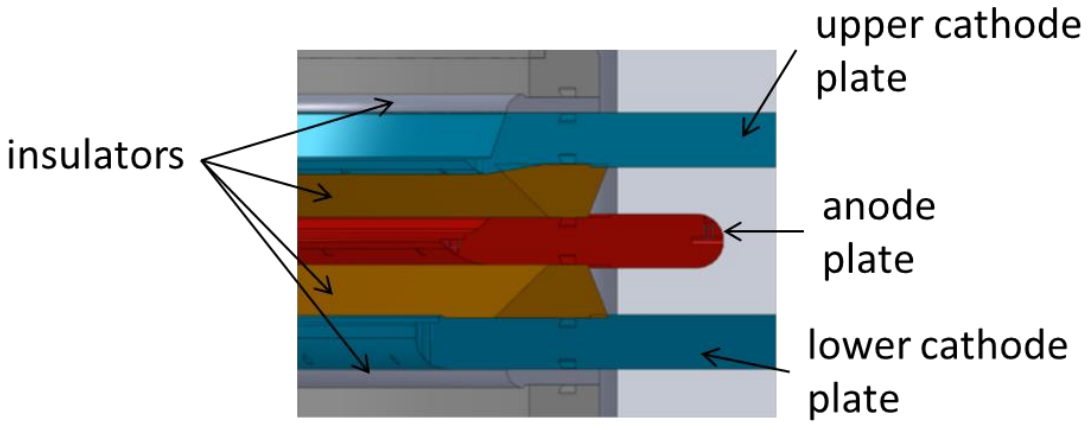

Figure 2.2: Cross section illustrating transmission line and insulating ring placement in the interaction chamber's wall.

This sealing design allows the perimeter of the transmission line stack to exist in atmosphere, removing the need for high voltage vacuum feedthroughs by allowing the cables to feed directly into the transmission line.

2.2. Current Source

The current source that feeds into the interaction chamber comprises one or more channels, where each channel is a capacitor, a high voltage spark gap switch, a water resistor, and six 59 Ω coaxial cables carrying the pulse from the channel to the transmission line interface. Furthermore, the switch and water resistor are housed inside a cylindrical "switch can" formed from aluminum, which can be filled with an insulator (typically sulfur hexafluoride, or SF_6) to insulate the high voltage surfaces. This switch can has a large, airtight port on its bottom that seals to the top of the capacitor, and has six ports on its lid for the discharge cables, as well as several auxiliary ports for its charge cable, current and pressure sensors, etc. The scaled system detailed in this thesis uses two such channels; the aforementioned 200 T system uses ten.

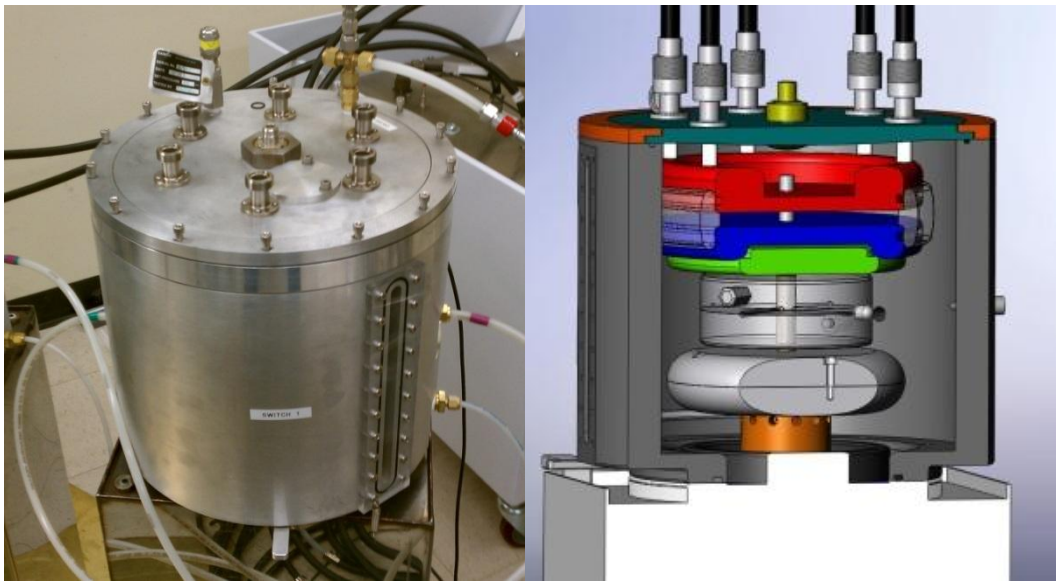

Figure 2.3: Current source. Left: Current channel #1 in lab. Small tab at bottom of picture is a shorting lever that prevents self-charging. Right: Solidworks cutaway. Bottom to top: capacitor, capacitor cap, cap/switch transition, switch, water resistor, lid, discharge cables. (5)

2.2.1. Capacitor

Figure 2.4: Capacitors sit on the ground, and switch cans are bolted to the top. Both capacitors rest on a copper sheet that ensures the two capacitors have a common connection at all times.

The capacitor is a 3.1 µF rectangular, oil-insulated capacitor, rated for holding off 100 KV. At its maximum charge voltage, this translates to a storage energy of 15.5 KJ ($E_{cap} = C \cdot V^2/2$). In the switch can is an aluminum capacitor cap, about the size of a soda can, which bolts to the center (positive) terminal of the capacitor. The capacitor's charge cable plugs into the side of this cap, and a saucer-shaped block of aluminum joins the top of the cap to the bottom of the high voltage switch. This saucer distributes the electric field from the capacitor's charge uniformly into the switch, preventing field gradients within the switch which could lead to undesirable switch behavior.

2.2.2. High Voltage Switch

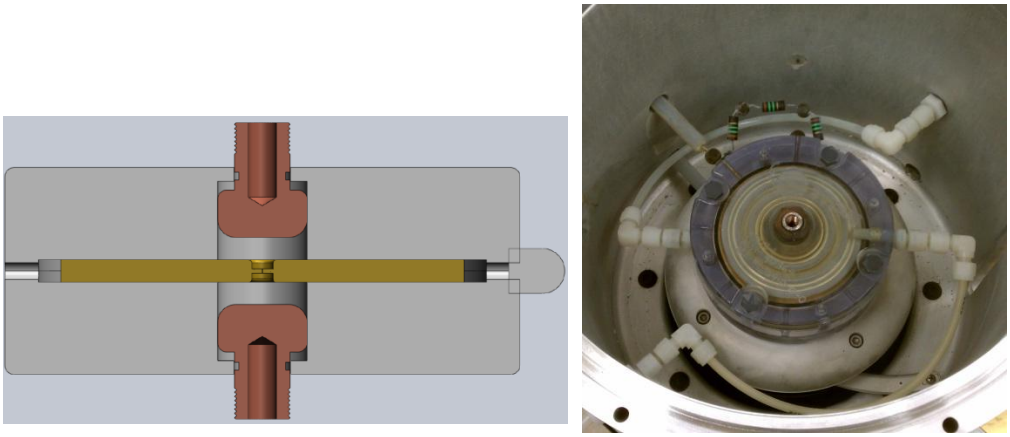

Figure 2.5: Left: Section view of Titan 40364 high voltage switch. Knob on right represents input for trigger pin. Right: Switch inside switch can (water resistor removed for visibility), switch pressure lines also visible.

To achieve the rapid (~10 ns) triggering of high voltages (≤100 KV), MegaGauss uses a spark gap switch, a technology commonly employed in pulsed power devices. (3) The configuration used in MegaGauss is a three-electrode switch, specifically, the Titan 40364 (L-3 Communications) spark gap switch. This type of switch relies upon Paschen's Law, a relatively simple mathematical model for electrical breakdown in gases. The maximum voltage before breakdown will occur is found by the formula which encapsulates Paschen breakdown:

$$V_B = \frac{a \cdot (pd)}{\ln(pd) + b} \tag{2.1}$$

where a and b are constants dependent upon the gas being discussed, and the product pd is the product of the gas pressure in atmospheres and gap distance in meters. As an example of values for a and b, consider air at atmospheric pressure, which has $a = 43.6 \times 10^6\ \mathrm{V/(atm \cdot m)}$ and $b = 12.8$. In the Titan switch, the three electrodes are all

azimuthally symmetric. The upper and lower electrodes, identical and facing each other, are knob-like electrodes. The lower electrode is connected to the positive end of the capacitor via the saucer structure mentioned before, and holds the full charge voltage (100 KV for a 100% shot). The upper electrode is connected to the load, and is thus the ground terminal. Placed equidistantly (¼" on either side) between these two electrodes is the third (trigger) electrode, which is plate-shaped with a dime-sized hole in its center. Two high value (~1 GΩ) biasing resistors set this electrode at mid-voltage between the capacitor and ground (50 KV for a 100% shot). Thus, the trigger electrode fits within the electric field gradient between the capacitor and ground electrodes.

Before firing, Paschen's Law is utilized to calculate the switch gas pressure necessary to hold off the charge voltage for the gap distance *d* between the trigger electrode and either knob electrode. When the trigger electrode receives a high-voltage (100 KV) pulse from a trigger generator (Maxwell model 40230 trigger amplifier), the electric field between the trigger electrode and the upper (grounded) electrode is suddenly increased beyond that which can be held off by the gas. If the gas pressure was properly chosen, this new electric field will be sufficient to break down the gas between the trigger and ground electrodes. The resulting arc joins these two electrodes, dropping the trigger electrode to ground potential, causing the breakdown to cascade to the electrode connected to the capacitor's terminal. This plasma channel formed from the arc closes the switch, and the capacitor discharges into the load. This process happens in parallel with other switches, delivering current from all capacitors simultaneously.

2.2.3. Water Resistor

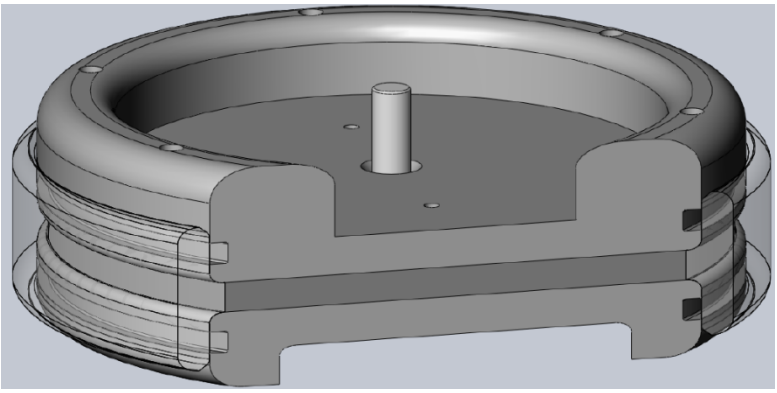

Figure 2.6: Water resistor cutaway. Center post is an insulated stud that allows the top and bottom plugs to bolt together. The conducting medium is in between the two plugs, and is contained by the clear plastic ring separating the plugs.

During a shot, excessive reverse voltage on the capacitors can be prevented by placing a damping resistor in series with the rest of the circuit. Thus, placed in each switch can between the spark gap switch and its discharge cables is a water-filled resistor which dissipates a portion of the oscillating energy. It is composed of three large circular stainless steel plates; two are plugs that confine the solution within an acrylic spacer of fixed length, and the third is a transition piece between the switch and water resistor's lower plug. This transition piece is designed to screw onto the top of the switch, while the upper plug of the resistor has six ports to accept the center conductors of the discharge cables. To set the resistance, a water solution with a specified concentration of a salt (e.g. table salt, copper sulfate) is used. To prevent air bubbles from being trapped inside the water resistor, the resistor components must be submerged in the solution during assembly. Values of the resistors used on MegaGauss run between 50 mΩ and 75 mΩ.

2.2.4. Discharge Cables

Energy is transported from the capacitor assembly to the interaction chamber by means of six 59 Ω coaxial cables (Dielectric Sciences, model # 2121). Each cable is 11 feet long, giving a signal propagation time of about 15 ns, based upon the dimensions and dielectric constant of the 2121 cable. On the switch can end of the cables are specialized vacuum-rated connectors to ensure confinement of the insulating SF_6 within the switch can. On the opposite side, the cables are terminated into exposed conductors, which plug into the chamber's transmission line.

2.2.5. Switch Can

An aluminum vacuum canister (Figs. 1.3-5), referred to as a switch can, houses the high voltage components of the channel's assembly. Within the switch can reside the positive terminal of the capacitor, the switch, and the water resistor, along with their transitional pieces and whatever cabling and tubing is required by these components. All components (excluding the cables and tubes) are built to be coaxial with the switch can. Since the current tends to flow on the outer surfaces of the components, the inductance of the switch can is estimated by means of the formula for the inductance of a coaxial line in free space:

$$L = \frac{\mu_0 l}{2\pi} \ln\left(\frac{R}{r}\right), \tag{2.2}$$

where l is the length of the coaxial line, and R and r is the radius of the outer and inner conductors, respectively. Thus, reducing switch can size is beneficial, as doing so will reduce inductance. As detailed in Appendix A.2, this coaxial inductance equation enables computation of switch can inductance when all interior components are in place.

2.3. INSTRUMENTATION SCHEMATIC

Current measurements are obtained by feeding voltage signals from current sensing coils (Ch. 3) within the switch cans and vacuum chamber feeding into a digitizing oscilloscope, after passing through attenuators that reduce the incoming voltage to a level acceptable to the 50 Ω input impedance in the oscilloscope (0 – 5 V_{RMS}).

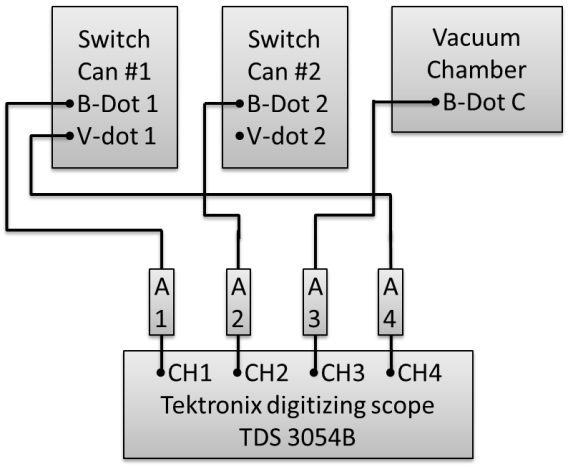

Figure 2.7: High-level schematic of instrumentation used on standard MegaGauss shots, such as the shots used to find the RLC parameters.

Concerning the frequency range of the instruments, the resonant frequency of the MegaGauss RLC is found to be approximately 150 Khz, several orders of magnitude below the cutoff frequencies of the attenuators, making these attenuators well-suited instrumentation for measuring the MegaGauss pulse. Furthermore, the TDS 3054B oscilloscope is capable of resolving signals up to 500 Mhz (analog frequency), at a 5 Ghz digital sampling rate. By the Nyquist theorem, we see the digital sampler can resolve up to a 2.5 GHz signal, well above the analog limit, proving the TDS 3054B can acquire up to a 500 MHz signal, 3 orders of magnitude faster than the MegaGauss RLC pulse. Interestingly, the instruments are not only able to resolve the RLC frequency clearly, but

also the higher frequency ringing in the discharge cables. Ringing amplitude is only a fraction of that of the main signal, but can easily be seen on the trace, demonstrating the instruments' ability to time resolve the signal. Typical oscilloscope settings for reading current sensor signals are 100 mV/div, representing ±500 mV across the ten-division vertical range. At these settings, the 9-bit resolution of the digitizer enables the trace to exhibit the main feature of the RLC pulse along with the smaller ringing feature (Fig 1.8).

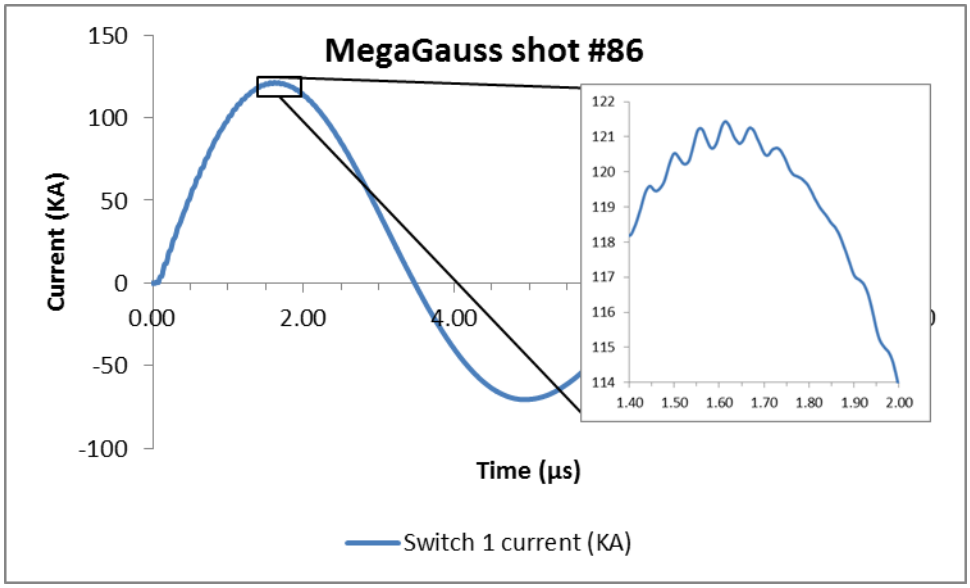

Figure 2.8: Detail view of cable ringing for Switch 1 at peak current.

	A1	A2	A3	A4
Attenuation	2X ± 0.1	2X ± 0.1	9.957X[1] & 10X ± 0.5	2X ± 0.1
Model	Tektronix 011-0059-01	Mini-Circuits CAT-6	Barth 142-NMFP-20B & Tektronix 011-0059-03	Mini-Circuits CAT-6
Cutoff freq.	2 GHz[2]	1.5 Ghz	30 GHz & 2 Ghz	1.5 Ghz

Table 2.1: Attenuator specifications used in typical MegaGauss configuration (e.g. system shots).

Perhaps the most critical attenuator is the attenuator stack (more than one attenuator is needed) that attenuates the voltage signal from the CVR during B-dot calibration (Ch. 3). If the attenuators used on the B-dots during calibration are not changed after the calibration, the CVR's attenuator stack determines the overall accuracy of the B-dot current measurements, since the B-dot attenuators' imperfections are taken into account by the nature of the calibration technique. With an attenuator stack of one Barth precision attenuator (9.957X), and two Textronix 011-0059-03 (10X ± 0.5) attenuators, the overall accuracy of calibration due to attenuator tolerance is computed:

$$V_{ATTEN} = V_{ACTUAL} \cdot \left(\frac{1}{9.957}\right)\left(\frac{1}{10 \pm 0.5}\right)\left(\frac{1}{10 \pm 0.5}\right) \tag{2.3}$$

$$= V_{ACTUAL} / \left(1000 \, {}^{+98}_{-101}\right) \approx V_{ACTUAL} / (1000 \pm 100) \tag{2.4}$$

[1] These attenuators are individually tested for their individual attenuation value during manufacturing, thus they do not have a typical nominal value with a tolerance. Consistent attenuation by this value over the course of 1000 shots is required by Barth's quality assurance process before shipment. (10) Thus, in the context of the other attenuators' tolerance in the stack, this tolerance is negligible.

[2] Specification for this model was unavailable, but a similar model (Tektronix 011-0059-03) had this

Into the precision resistor (CVR) with resistance 0.004987 Ω, and an average after-attenuator voltage of 0.600 V (Appx. B), the current measurement is:

$$I = 0.600\ V \cdot \frac{(1000 \pm 100)}{0.004987\ \Omega} = 120 \pm 12\ KA, \tag{2.5}$$

from which we obtain the possible error on current measurement due to attenuator tolerances.

Accuracy of the voltage signal itself due to voltage divisions of the oscilloscope are unlikely to modify this value significantly, since the TDS 3054B is capable of ±2% accuracy in voltage measurements. For a setting of 500 mV/div, this is an error of ±10 mV/div. For a 0.600 V signal, this error is:

$$voltage\ error = .600\left(\frac{\pm 10\ mV}{.500}\right) = \pm 12\ mV. \tag{2.6}$$

Propagation of this error into Eqn. 1.5 gives:

$$I = (.600 \pm 12\ mV) \cdot \frac{(1000 \pm 100)}{0.004987\ \Omega} \approx 120 \pm 15\ KA\ (12.5\%), \tag{2.7}$$

yielding the total error of from both oscilloscope and attenuator imperfections. These reflect the error analysis for a 50% energy shot; for a shot on the MegaGauss system at 100% energy, voltage divisions are 1.00 V/div for the B-dots (channels 1 – 3), and 200 mV/div for the V-dot trigger (channel 4).

Chapter 3: Current Sensors (B-Dots)

3.1. Calibration of B-Dots

Before any significant performance tests can be executed, an initial measurement of the current provided by each capacitor/switch assembly is necessary. Once calibrated scale factors relating current with sensor voltage are acquired, accurate current measurements may be obtained from these sensors. Such a current sensor (B-dot) is desirable because it measures current without the addition of a sensing element in the main circuit; it is coupled to the current via the current's magnetic field. These B-dots, one per switch can, are magnetic pickup coils that produce a voltage linearly related to the change in magnetic field through its cross-section. However, this relation between the voltage and field must be calibrated if an accurate measure of current is to be obtained. This demands an accurate method of measuring current other than these pickup coils; in this case, a low inductance, calibrated, current viewing resistor (CVR) is placed into the circuit (Fig 3.1).

The voltage across the CVR is measured, and Ohm's law allows simple computation of the current passing through the CVR. By firing one capacitor/switch assembly at a time, it is possible to relate the B-dot voltage with that across the CVR. Both B-dot voltage and CVR voltage are linearly related to the current, allowing a proportional calibration factor to be computed. With this proportionality constant in play, the B-dot can be related to true current; and thanks to its decoupling from the main circuit, experiment conditions (e.g. electrical loads, undesired electrical breakdown, etc.) do not prevent current measurement. This sensor is useful as a diagnostic, as the typical RLC response for MegaGauss may be characterized, then compared with later shots to verify continued proper operation.

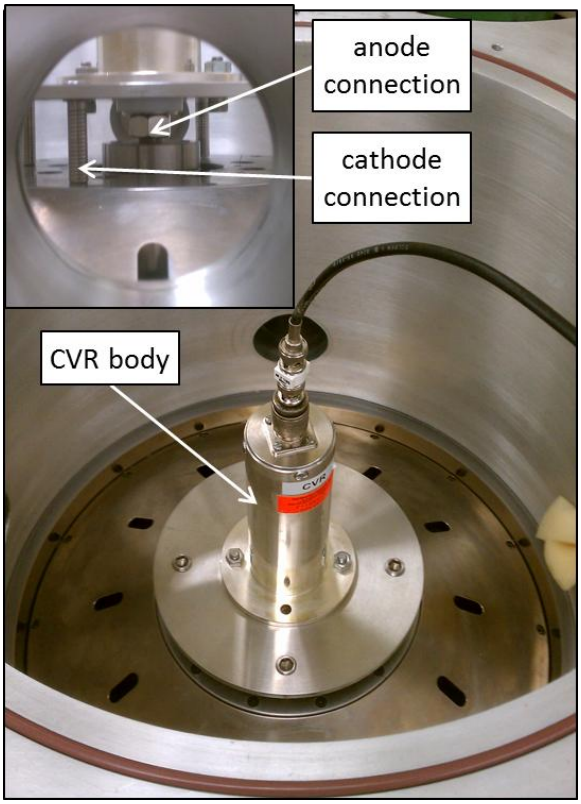

Figure 3.1: CVR placed into the interaction chamber during B-dot calibration. Inset: side view through diagnostic beam port illustrates electrical contacts.

A specialized fixture holds the CVR in a position on the transmission line in the interaction chamber such that the entire current provided by the system passes through the CVR. The voltage across the CVR, read through a N-type terminated coaxial cable, is sent into a digitizing oscilloscope for analysis after passing through a strong (1000X ± 100X) attenuator circuit on the oscilloscope side of the signal cable. Alongside this signal, the B-dot voltage signal is overlaid, and a scale factor may then be determined using the following formula for the B-dot scale factor:

$$k_{B-dot}\,[A/V] = \left(\frac{V_{CVR}}{R_{CVR}}\right)/V_{B-dot} \tag{3.1}$$

Since the percentage of total current from each switch is not known, an accurate calibration may not be obtained unless each capacitor/switch assembly is fired into the load alone. Furthermore, the CVR used for this calibration is unable to withstand the current from two or more capacitors firing at the typical 50% energy. In practice, calibration in MegaGauss is only done at low (~25 - 50 KV) charge voltages, as full energy will have the same destructive effect on the CVR as firing multiple capacitors.

3.2. B-DOT SENSOR PRINCIPLE

While the concept of the CVR, being a simple resistor, is simple to understand, the concept of the magnetic field sensor (B-dot) is slightly more complicated. In fact, for reasons that will be apparent in the following explanation, the sensor is actually measuring the time rate of change in magnetic field, and not the magnetic field directly, hence the term B-dot.

B-dots are an excellent general-use magnetic field sensor, and are used extensively in pulsed power systems, as they are simple to build, place, and calibrate. (3) The physics governing the functioning of B-dots is easily understood by looking at the well-known Maxwell-Faraday Law (law of induction) in integral form:

$$\oint_{\partial S} \vec{E} \cdot \overrightarrow{dl} = -\iint_{S} \left(d\vec{B}/dt\right) \cdot \overrightarrow{dS} \tag{3.2}$$

In the case of a single-turn solenoid, which is the construction of the B-dots used in MegaGauss, the curl of the electric field will provide a voltage difference across the two ends of the loop. Assuming a spatially uniform magnetic field, which is reasonable since the diameter of the circular cross section of the B-dot is approximately ¼", and the

cross section the field fills is several inches in width, and neglecting fringing fields, these integrals may be evaluated simply:

$$E \cdot 2\pi a = S \cdot dB/dt \Longrightarrow B \propto \int V \cdot dt \tag{3.3}$$

where a is the radius of the pickup loop, S is the cross sectional area of the loop, and V is the voltage across the terminals of the pickup loop. Since the magnetic field may induce currents in the signal cable, neglect of fringing fields may not be perfectly defensible, but it is a necessary approximation to simplify the discussion of B-dot operation. Fortunately, the nature of the calibration technique absorbs any additional linear contributions into the B-dot's scale factor. The result (Eqn. 2.3) shows that the time integral of the voltage is linearly proportional to the magnetic field being sampled, which, as is known by Ampere's Law, is linearly proportional to the current producing the magnetic field.

$$\vec{\nabla} \times \vec{B} = \mu_0 J + \mu_0 \varepsilon_0 \frac{\partial \vec{E}}{\partial t} \tag{3.4}$$

Therefore, by time-integrating the B-dot's voltage signal, it is possible to obtain a signal proportional to the current passing through the center of the switch can. Once all B-dots are calibrated, a consistent reading of current may be obtained without disrupting the current.

3.3. Determination of B-Dot Calibration Factor

In solving for the calibration factor of each B-dot, the typical approach of computing current from CVR voltage and scaling the integrated B-dot to match the CVR current reading was used. When MegaGauss was first assembled at UT and operated, this was the first priority, after validation of total system operation was established. Firing

into the CVR with each switch, several calibration shots were taken at 50 KV. These data were used to compute calibration factors for each B-dot. Of course, if a B-dot is ever replaced or repositioned, greatest accuracy demands that the calibration be redone. If a calibrated load B-dot is available, it is possible to read the current into the load from a given channel, and thereby reverse calibrate its B-dot. However, best practices advise against this, as use of the factory-calibrated CVR reduces the inaccuracy introduced into the process. Although, for an estimate, it may be acceptable to use this secondary, simpler calibration method until the CVR can be placed into the interaction chamber for a more accurate calibration. For the data points used in the initial calibration of the switch B-dots, please refer to Appendix B.

Chapter 4: Typical Failure Modes

Normal operation has been established, and we will now review several interesting failure modes noted across the history of operation of MegaGauss. The primary failure diagnostic is the B-dot data, although occasionally the sound of the discharge varies, and can indicate a failure. Since this auditory diagnostic tends to be quite subjective, we will ignore this and focus only on B-dot readings.

Ideally, the B-dot reading at the load should have the same decaying sinusoid shape as the switch B-dots. Also, the expected waveform characteristics are known, and significant variation from these is a strong indication of failure.

4.1 Breakdown in Interaction Chamber

After the initial calibration of the switch B-dots, the first series of tests probed the ability of the chamber to fire in vacuum. It was found that the chamber has an intermediate pressure range throughout which breakdown occurs within the chamber, shorting the load and often preventing attainment of peak field.

This is probably the most recorded failure in MegaGauss, and was noticed first while attempting to fire at chamber pressures lower than atmosphere. Early in the life of MegaGauss, it was found to be capable of consistently discharging at least 50 KV into a standard load (Helmholtz coil, Figs. 5.2-3 and Appx. A.3), as long as the pressure was either approximately atmosphere, or below 20 milliTorr of background pressure. The conclusion from this behavior was that the intermediate pressure range presented the opportunity for Paschen breakdown, a well-known phenomenon in high voltage systems (§2.2.2). This breakdown produces a plasma channel that allows current to bypass the load, and this short circuiting of the load is easily observed in the form of a sudden break of the load current trace from its expected sinusoidal behavior (Fig. 4.1).

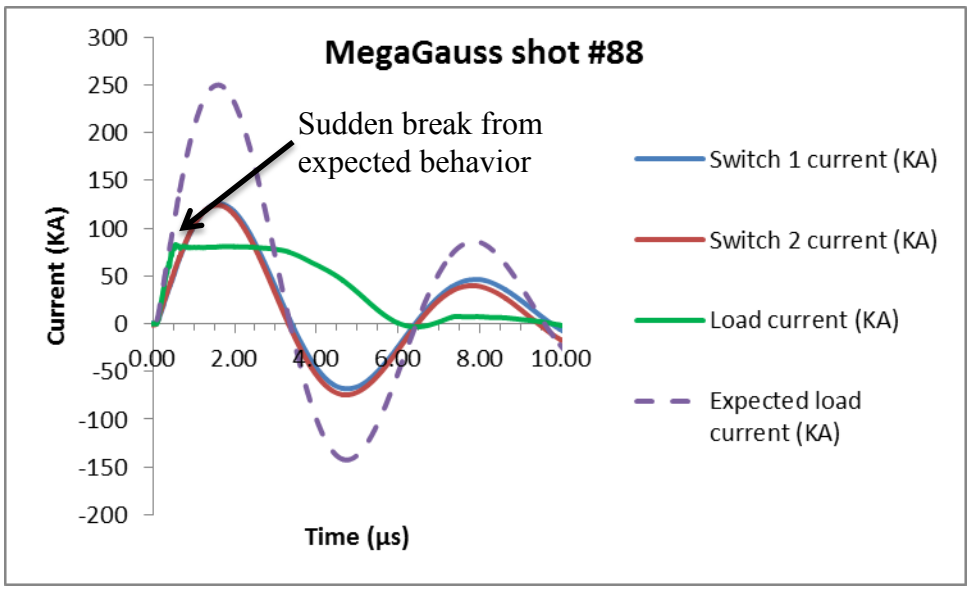

Figure 4.1: Signature of chamber breakdown failure. Switch currents do not change, but load current suddenly deviates from expected behavior.

In the example above, about 0.5 µs after the pulsed power fires, the load current abruptly discontinues its expected behavior, indicating that the load current has been diverted through another path. It is also interesting to note that the switch current measurements indicate normal operation (i.e. same frequency and decay), even though their discharge path has changed. Since most of the inductance in each switch-to-load circuit is found before the interaction chamber (Appendix A.1), and diversion of current away from the load into a breakdown arc does little to change the overall circuit characteristics, this lack of change in switch current behavior is reasonable.

Lastly, it should be noted that this breakdown is not always an indication of a failed shot. If breakdown occurs after peak current, and therefore field, is reached, this breakdown is negligible, since peak magnetic field has already been produced, and the

shot may be considered a success. However, if this breakdown presents itself before peak current, it is a critical failure and must be addressed.

Detailed characterization of the chamber's pressure response in the context of a 50% pulsed power shot was obtained by varying the background pressure in the chamber and observing the load current. A sudden break (e.g. Fig 4.1) indicates shorting of the load, and the pressure at which the breakdown occurred is marked as a pressure that leads to breakdown. These pressures lie approximately between 10^{-4} Torr and 400 Torr (intermediate pressure regime, Fig 4.2). Thus, to reach peak current for a 50% shot (~240 KA) in vacuum, the background pressure in the interaction chamber must be at most 10^{-4} Torr.

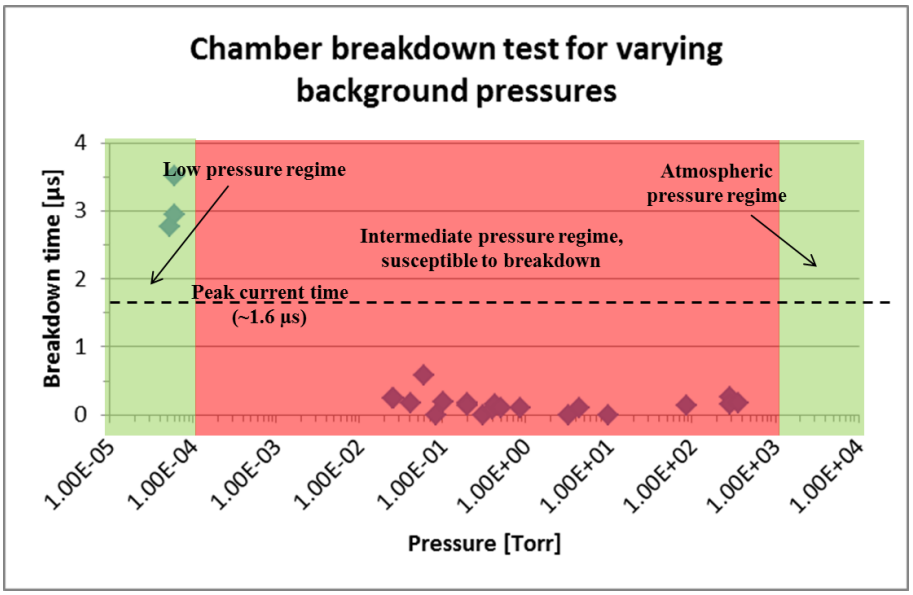

Figure 4.2: Operating pressure range of MegaGauss interaction chamber. 50 KV shots were fired at various background pressures, and time elapsed before breakdown was plotted (Appx. C). If breakdown time exceeds time to peak current (~1.6 µs), the shot may be accepted as successful.

Although breakdowns were observed at lower pressures (low pressure regime, Fig 4.2), these breakdowns occurred after the time to peak (1.6 μs), and these shots are considered successful.

Initially, unexpected breakdown was observed in the low pressure regime, and always occurred sometime after polarity reversal (i.e. after peak current). Whereas shots fired in the immediate pressure regime consistently break down before peak current, these shots in the low pressure regime reach peak current, and often break down when current direction reverses. It is hypothesized that when this reversal occurs, the dielectric rings insulating the transmission line plates (Fig 4.3), which are shaped to prevent breakdown for positive polarity, suddenly become susceptible to this breakdown upon polarity reversal.

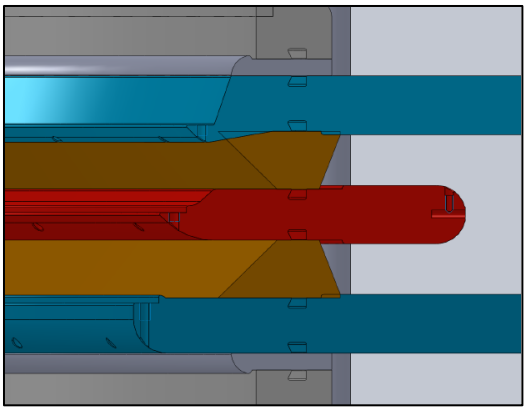

Figure 4.3: Trapezoidal dielectric rings (trapezoidal cross section) separate transmission line plates (top and bottom: cathode, middle: anode), and prevent electron cascades from rogue emitted electrons.

The trapezoidal dielectric ring separating the tri-plate elements is oriented such that electrons emitted from the cathode and accelerated by the electric field between the cathode and anode strike the anode rather than the dielectric ring. If the latter takes place,

and the secondary electron emission from the ring is sufficient for positive feedback, the dielectric becomes positive, increasing the accelerating field, thus resulting in a growing electron flux from the cathode to the dielectric. (3) This can eventually result in a breakdown capable of damaging the dielectric, and will certainly short the load current. Since polarity reversal implies that the anode becomes the cathode, the angling of the dielectric no longer serves its purpose, presenting a possibility for breakdown. While this polarity-dependent arcing seems to be a reasonable explanation, this has not been vetted by experiment since post-peak breakdown does not interfere with operational success.

To summarize these results, we can say that critical (before peak current) breakdown occurs for pressures within the intermediate range, and gives an upper limit on the pressure the chamber's vacuum system should allow. According to the available data, it is necessary to establish a vacuum pressure of 10^{-4} Torr or better to ensure successful high field shots. To enter and operate well within the low pressure regime within a reasonable time after sealing the chamber, a high vacuum pump is required. In the case of MegaGauss, a turbomolecular pump (Oerlikon Leybold TMP-50) has been attached to a chamber port to provide quick access to this low pressure regime. This allows the system to reach an acceptable pressure within approximately 30 minutes.

It should be noted that a significant caveat is still in play concerning the interpretation of this data. These shots were taken at half of full system energy (50 KV, as opposed to the maximum 100 KV). With higher voltages, it is possible that the pressure necessary to hold off breakdown will drop even further than that recorded by this experiment (Fig. 4.4). When the time comes to operate the system consistently at higher currents (i.e. full energy shots), a new test should be executed to reestablish or unseat the present pressure ranges.

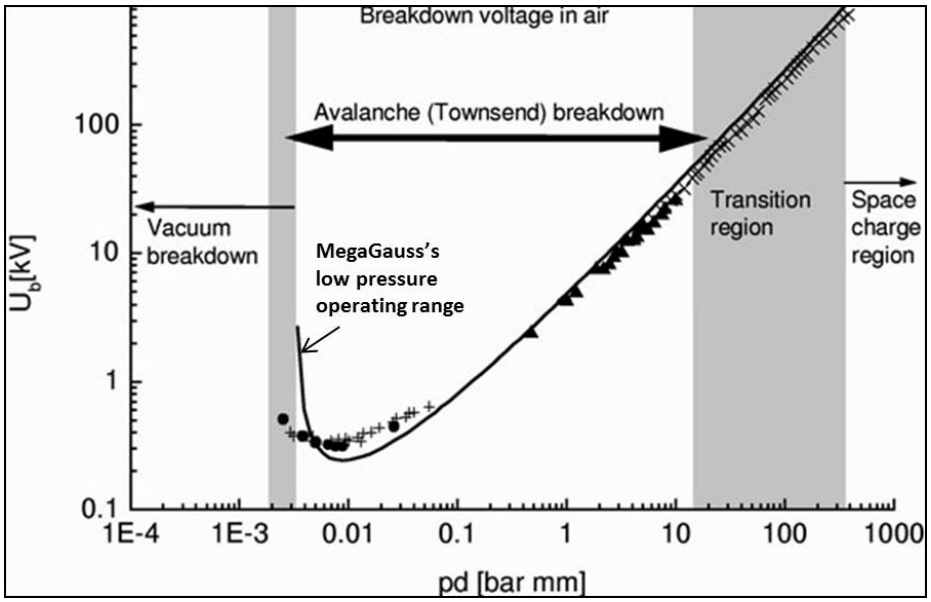

Figure 4.4: Voltage across chamber components rises linearly with peak current ($V = L \cdot \partial I/\partial t$). To hold off this increased voltage, pressure (p) must decrease, assuming breakdown gap distance (d) stays constant. (3)

4.2. BREAKDOWN IN SWITCH CAN

Switch containment vessels (switch cans), are also susceptible to arcing, although it is not as common due to the sulfur hexafluoride (SF_6) insulating gas present inside the cans. Most frequently, the arc travels from the top of the water resistor to the bottom of the lid, avoiding the discharge cables. The diagnostic for this failure is more involved; not only does the load current trace suffer, but that of the failed switch is affected significantly as well.

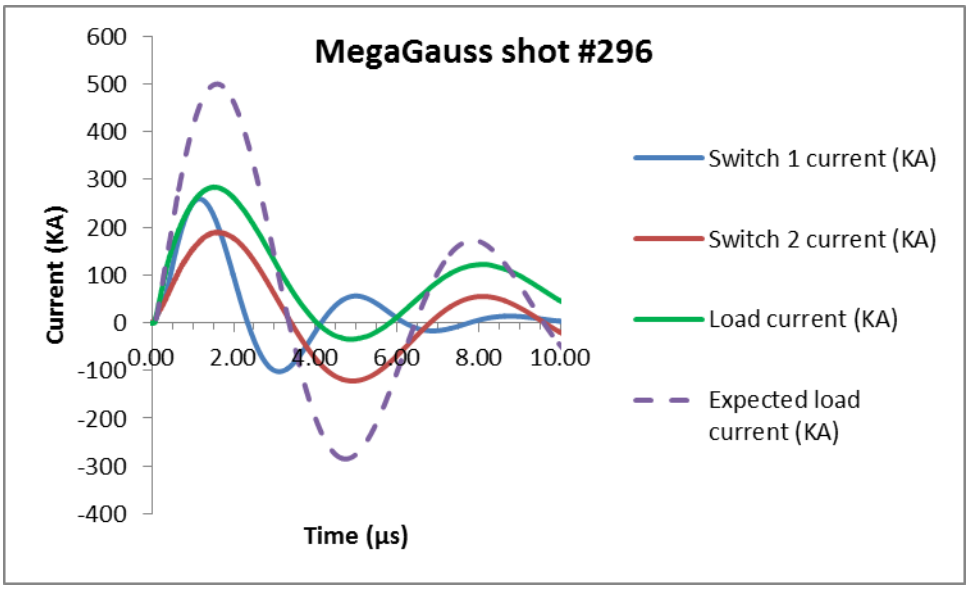

Figure 4.5: Drastically different oscillation period in Switch #1's current indicates inductance of Channel #1 has been significantly reduced. Notice Switch #2 is behaving as expected, suggesting only Switch #1 failed.

In Figure 4.5, the load current appears to miss the mark almost immediately after firing, and the current through Switch #1 suddenly changes its oscillation period. This offers a stark contrast with the breakdown in the interaction chamber. While chamber breakdown did not affect the switch current readings, in this case of a switch can breakdown, inductance changes drastically, since the discharge cables feeding into the interaction chamber have been short circuited. This results in a huge deviation of inductance from regular parameters, and according to the expression for ω_0, such a change would strongly affect the oscillation frequency of the circuit.

Thus, when the oscillation frequency of a switch's current changes drastically, this is a good indication that the switch can has experienced an electrical breakdown. As is the case for chamber breakdown, if this breakdown occurs after peak current, the shot is not a wasted effort. However, in the case of switch can breakdown, immediate

corrective action should be taken regardless, since much of the switch can is constructed with aluminum, rather than the more robust stainless steel that composes the chamber's transmission line. These aluminum surfaces tend to exhibit significantly more damage (e.g. sputter) than their stainless steel counterparts, and allowing these damaged surfaces to remain will only increase the changes of further breakdown and further damage.

4.3. Premature or Improper Switch Firing

This failure mode is unusual, but can be encouraged by lack of coordination of charge voltage and switch pressure. Because the high voltage switches function by means of a controlled Paschen breakdown, an insufficient switch pressure will not hold off the charge voltage, and the switch will self-trigger. On the other hand, too high a pressure will prevent the trigger voltage from breaking down the gas in the switch, thereby delaying or preventing the firing of the switch. Both of these errors result in uncontrolled firing of the system, which is an unacceptable scenario. Finally, it may be possible that dirty or damaged interior switch components would increase the likelihood of undesired breakdown, even with the appropriate switch pressure. Although this is considered a possibility, it has not yet been noted over the course of the operation of MegaGauss.

Chapter 5: Effects of Extensive Firing

The MegaGauss apparatus is designed for long-term use, which means several hundred shots with minimal maintenance should be possible. This is very different from larger pulsed power devices such as Sandia's Z Machine, which must be extensively refurbished after every shot. Even so, there are several undesirable and/or interesting effects from long-term operation of MegaGauss, and those will be detailed here.

5.1 Dust Buildup

5.1.1. Switch cans

After several dozen shots, buildup of a fine white powder within the switch cans is apparent throughout. According to Brian Stoltzfus, a Sandia National Laboratories engineer, this is a common effect seen in pulsed power devices that use SF_6 in high voltage environments, and is not considered a harmful substance. This thin layer of powder has not been observed to be causative of failures, neither here nor at SNL. However, removal of this coating is standard procedure after several dozen shots, if only to prevent excessive accumulation.

5.1.2. Switches

Particulates also appear inside the high voltage switches. Unlike the switch cans, these do not contain SF_6; they only contain Ultra-Zero grade (purified and dry) air. In this case, it is likely that arcing in the switch (a necessary arc since this is the principle of the switch) disturbs layers of oxides on the surfaces of the electrodes, releasing particulates into the air within the switch. Thus, when the switch is disassembled, a copper-colored deposit on the electrodes and the interior of the switch housing is a common sight. As with the switch cans, a lint-free cloth may be used to clean the switches. However, it is

important to note that isopropanol, if used to clean components, must not come into contact with the switch housing's plastic surfaces, as this chemical will result in crazing of those surfaces. In the case of both switch can and switch particulates, the levels of buildup from one hundred shots or less have not been correlated to faulty operation.

5.1.3. Chamber

Within the interaction chamber, particulates of another kind are observed. These particles appear as both powdery deposits and small metallic flakes, usually having a light gray color. Due to the color, and observed damage on current-carrying aluminum elements found on the coil clamp after firing several shots, it is expected that these are primarily aluminum particles released by ablation due to arcing at contact points, especially the contact surfaces between the coil clamp jaws and the coil. This hypothesis is supported by the easily observed deposition of aluminum on the base of the coil after firing (Figure 5.1).

Figure 5.1: Aluminum deposition on coil feeds.

These particles are typically cleaned away from the interaction chamber after approximately twenty shots, since it is thought that these larger flakes of metal may

provide electric field enhancements, leading to increased likelihood of undesirable arcing. When higher currents are achieved with the 200 T system, magnetic pressures will be capable of exploding the coil, and metallic debris will become a greater concern, likely necessitating cleaning of the chamber after every shot.

5.2 Coil Clamp Loosening

The coil clamp designed to hold the coil onto the conical transmission line during the shot is susceptible to loosening due to two factors: magnetic pressure and contact surface damage. The first factor is well known for a magnetic field, and has the expression:

$$P_B = \frac{B^2}{2\mu_0}$$

With the two-capacitor system being discussed here, firing at half energy (~250 kA peak current) this magnetic pressure between the coil feeds is in the range of 250 MPa, which, over the surface area of the flat feeds of the coil (.30" x .50"), produces a separation force of about 47,000 Newtons (~10,600 lbf). Of course, this force is delivered for less than a microsecond, and usually only results in a deformation of the coil.

In addition to this tremendous force upon the coil clamp, the contact surfaces of the clamp, being subjected to such a high current density, are susceptible to sputtering during current flow. This sputtering ablates a layer of material from the contact surface. It is thought that this is the primary source of particulate buildup inside the interaction chamber. This removal of material effectively reduces clamping pressure on the coil, allowing the coil to become loose. This poorer contact also reduces the quality of the

electrical contact, aggravating the sputtering problem if not addressed. Typically, shims are placed into the coil clamp to compensate for this reduction of material.

Clamping force on the coil is threatened by these two effects (magnetic pressure and contact surface degradation), but awareness of these problems, and preventative maintenance have been found to extend the useful lifetime of the coil clamp significantly, at least for lower energy shots.

5.3 COIL DAMAGE

After only the first shot, the coil will display at least one of several effects. As the peak current in each shot is increased, these effects manifest themselves increasingly strongly. For example, a 50% energy shot may result in aluminum deposition on the coil, but it will not distort the shape of the coil (at least not on a new coil's first shot). For an 80% shot, aluminum deposition will be present, in addition to significant coil distortion effects.

5.3.1. Magnetic Pressure

Magnetic pressure, as mentioned in a previous discussion, is responsible for loosening of the coil clamp over the course of several shots. The separation force caused by magnetic pressure is absorbed by the coil clamp, but only where the coil clamp clamps over the coil feeds. Where the coil is not reinforced, it expands according to the influence of magnetic pressure forces. This is most noticeable at the coil feeds (the coil's straight "legs"), at the point just before the feeds bulge out to form the cylindrical portion of the coil. This is because the influence of the interior pressure drives the deformation towards a circle, and the feeds, not following that shape, deform to become part of the circularly shaped part of the coil. This expansion of the feeds is noticeable for 50% energy shots,

but only over the course of at least a dozen shots on the same coil. With an 80% energy shot, the deformation is dramatically obvious after a coil's first or second shot. After this, the coil is nearly useless, since the deformation is so great that the coil clamp can no longer press the distorted feeds sufficiently to maintain satisfactory contact pressure. Figure 5.2 shows the distortion of the feeds of a coil subjected to two 80% energy shots.

Figure 5.2: Axial profiles of an unused coil (left) and a coil subjected to two 80% energy shots (right). Note the spreading of the feeds just above the clamped region (coincident with aluminum deposition), the ellipticity of what originally was the circular portion of the coil, and the increased radius.

5.3.2. Mutual Attraction

In addition to this expansion of the feeds, the two cylindrical portions of the coil are subject to mutual attraction between themselves. An identical effect is seen when two parallel wires in close proximity, carrying current in the same direction, bend toward each other. This mutual attraction is caused by the Lorentz force, as the magnetic field of one wire draws the current in the other, and vice versa, resulting in a force that pulls the

wires closer together. This effect is most noticeable for high energy shots, although 10 - 20 low energy shots can produce similar deflections.

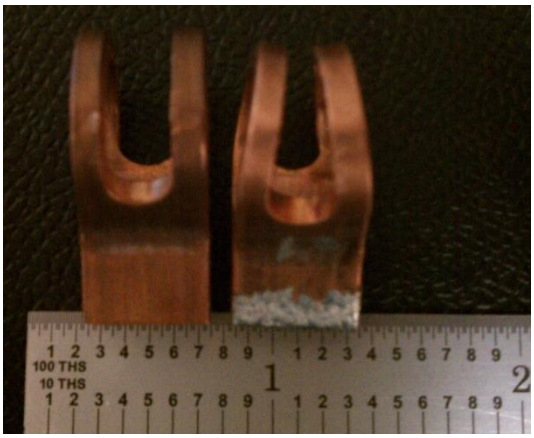

Figure 5.3: Lateral view of the same coils pictured in Fig 5.2. Mutual attraction between the two current loops causes them to pinch together. Also note deposition of aluminum onto the formerly clamped portion of the feeds.

5.3.3. Contact Degradation

Finally, it is typical for the contact surfaces of the coil to be coated with a layer of aluminum (the coil clamp material), due to what is expected to be melting and sputtering of aluminum during current flow (Fig. 5.3). This material transfer is corroborated by the loss of material on the contact surfaces of the coil clamp. Eventually, this buildup, not being well deposited onto the coil surface, can result in a loose coil connection due to what is essentially debris between the coil clamp and the coil. The typical solution to this, as mentioned elsewhere, is a tightening of the coil clamp to restore contact pressure.

Eventually, the coil will become useless due to one or several of these damaging effects. Depending on the energy of the shots the coil is subjected to, its lifetime may be twenty or more shots, or only one or two. Furthermore, as the MegaGauss system is upgraded, a critical current is expected that will cause the coil to be torn apart due to

magnetic pressure. As of yet, with a highest recorded current of 450 KA (Shot #303) into a ½" ID coil made of ⅛" thick, ½" wide copper (Figs. 5.1-3, Appx. A.3), this has not happened.

For 450 KA, the field produced by a Helmholtz coil, based on the coil's geometry (Appx. A.3, Eqn. A.2), is 32 T. For a smaller coil with an inner diameter (ID) of 3/8 in (~1 cm), the field should reach 42 T. At the time of publication of this thesis, two shots (#309, #311) have been fired into such a coil, both at currents between 450 KA and 500 KA, as indicated by the current measurements of the two switches' B-dots. Interestingly, this exceeds the theoretical maximum current, casting some doubt on these initial results. Further confirmation is necessary before considering this to be the highest recorded current. Assuming this current is indeed passing through the coil, 450 – 500 KA will produce between 42 and 47 T within the 1 cm ID coil. Magnetic field may be further increased by continuing to reduce coil size, but this complicates the next phase of the pulsed magnetic confinement of laser plasma experiment summarized in the introduction, in that diagnostic beams and nanocluster injection apparatus must have sufficient space within the coil to operate properly.

Chapter 6: MDSplus Archive Structure

6.1. Introduction to MDSplus

Due to the expansive volume of data that will eventually be collected by MegaGauss, well-defined data storage architecture is crucial. Such an archive requires a robust data structure that can store all data associated with each shot, regardless of type. This ensures that all relevant data for each shot will be accessible from a single location, which simplifies storage and post-shot access and analysis. Such a data structure must be expandable, readable, reasonably ordered, and able to store different data types within the same structure (e.g. single numbers, text, vectors, etc.)

Typically, the storage structure utilized is a spreadsheet format. This data structure, essentially a matrix, is useful for simple purposes, and is somewhat adaptable to complicated data. However, mixing vectors, individual numbers (e.g. shot number), and text can be disorderly in a matrix format, since a vector will occupy many indices, while the single number will only need one. Text will have to be dealt with on a character-by-character basis, or typecast to a form which can be sent into the spreadsheet. Furthermore, a spreadsheet requires consistent data formatting, with labels to indicate what data is stored in each cell. If some data sets have more cells than others, difficulty can arise when reading the data. For example, imagine a spreadsheet with three data cells, each containing a voltage measurement. A program can be written to read these data cells. However, suppose a fourth voltage sensor is added, requiring a fourth data cell. The reader program must discern which type of file is being read: the three or four cell format. Suppose now the four sensors are reversed, so sensor 1 becomes sensor 4, 2 becomes 3, and so forth. The reader program now has three formats to differentiate. In the case of MegaGauss, it is expected that dozens of differently formatted data sets will

be used, with the further complication that some of the data will be vectors or text rather than single numbers. This format differentiation problem arises from the lack of a conventional data structure that does not depend on data type or volume. These distinguishing characteristics, or metadata, should be associated with each object stored in the data set, which will provide order in an expanding, shifting data structure.

An example of a data structure that is designed with such inherent metadata is a database. Databases, in addition to having the capability to store large volumes of data, require metadata during their initial definition. Thus, the very act of creating the data template establishes an order that lends structure to the data. This simplifies data access, since the reader program can search for a particular metadata characteristic (e.g. "oscilloscope 2, channel 1"), rather than picking, for example, the fifth column of a spreadsheet. Even if the database changes, the reader program only regards the metadata, and is not concerned with how the database stores the information associated with that metadata.

Implementation of such a database structure is accomplished in MegaGauss by way of a "single, self-descriptive, hierarchical structure" called MDSplus. Developed jointly by the Massachusetts Institute of Technology, the Fusion Research Group in Padua, Italy (Istituto Gas Ionizzati and Consorzio RFX), and the Los Alamos National Lab, MDSplus was designed for use in large scientific experiments in which vast data archives are maintained. Primary among these are those derived from magnetic fusion experiments. MDSplus is freely available online. (6) MDSplus is a tree-form data structure whose metadata is accessible by several common methods, regardless of the data type. The great strength of the tree structure is the hierarchical layout, which immediately allows intuitive organization of data. Of course, the data itself may not

actually exist on the storage medium as a tree per se, but this does not concern the user, as the tree is the high level structure used to access or manipulate the data. Furthermore, the MDSplus format allows the user to query the data type, tree location, and more, meaning the tree can be scanned, then fully reconstructed and displayed on a user interface, without needing knowledge of the underlying structure of the tree. Versatility is another strength of the MDSplus format, in that several programming approaches may be taken to extract data. These include command line and GUI applications packaged with the MDSplus distribution, or IDL, MATLAB, Labview, etc. These capabilities can exist in spreadsheets as well, but attempting to implement such a tree structure within a spreadsheet effectively duplicates the functionality and versatility that MDSplus has already accomplished.

In the context of the expanding data sets from MegaGauss, a hierarchical, expandable structure is very desirable. When combined with the robustness that the metadata provides, MDSplus appears to be suitable archive solution for MegaGauss. However, the native MDSplus methods are written in a programming language that is not directly compatible with Labview (National Instruments) software (the language of MegaGauss's main control program), making it necessary to have a software bridge to access the MDSplus methods. This software bridge, named mdscwrap, is made available online by UW-Madison's Pegasus Toroidal Experiment (7). This software set provides an interface, or wrapper, between MDSplus and Labview via the C programming language. By combining MDSplus and UWM's wrapper code, it is possible to implement an MDSplus tree in Labview with little extra coding.

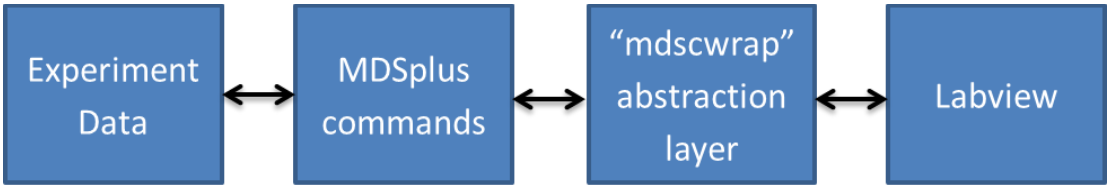

Figure 6.1: Information abstraction between components of data archive program.

Before discussing the specific application of MDSplus to MegaGauss, we will review the architecture of the tree data structure and how MDSplus implements this, such as node naming conventions, etc. We will also see this architecture illustrated in an example MDSplus tree, and highlight some of its associated metadata. After this background is established, we will focus on the main topic of how this MDSplus structure is engineered into Labview code, and integrated with the main MegaGauss control program. Finally, we conclude with a description of a novel data reading program that displays the tree structure, reads the data from the tree, and plots and analyzes that data.

6.2. TREE STRUCTURE BASICS

To begin the examination of how we use MDSplus to archive shot data, let us first understand the form in which the data is organized, as a tree is a more sophisticated data structure, at least compared to a spreadsheet. Fortunately, a tree structure is somewhat intuitive, as long as the question as to how the data is actually stored onto the storage media can be neglected; the discussion should focus on how the data is organized in the higher-level tree structure. By issuing commands to the MDSplus interface, MDSplus can be invoked to extract the desired information and synthesize the stored data into relevant information.

6.2.1. Root

At the base of each tree is the root path. For MegaGauss, the name associated with the root is *TOP*. Above root is the name given to the tree upon its creation (e.g. *datatree*). All positions on the tree (each position is called a node) will contain *datatree* at the beginning of their designated name. Indeed, because of the naming convention used in MDSplus, the node names are sufficient for determining the entire structure of the tree. Beneath the *TOP* node lie all other positions on the tree.

However, specifying the tree name is not sufficient to specify a data set. Since MDSplus is designed for storing experiment data, which is typically separated into separate shots (runs, trials, etc.), MDSplus has an individual tree for each shot. Thus, to point to a data set from shot 5, for example, mentioning *datatree* must be combined with a reference to shot 5, specifying the tree for shot 5. These specifications of tree name and shot number must occur in parallel during any operation in which a tree is modified or created. It should also be mentioned that shot -1 refers to the template tree, a special tree that provides the template for new shots. This template may be altered at any time, and future shots will reflect those changes. For example, if a new sensor is added to the experiment apparatus, the user must only add a new node into the template, and subsequent shots will have that additional node into which data.

When a new shot is created, three files are created: a tree file (*.tree), a data (*.datafile) file, and a characteristics (*.characteristics) file. The first provides the tree structure, the second holds the actual data, and the last contains the metadata. As mentioned in the introduction, it is not necessary to understand or even be aware of these files; all that matters is the accessibility of the files and the capability of issuing commands to the MDSplus abstraction layer to access the data stored in these files.

Further details of how MDSplus modifies and creates trees can be found on the MDSplus online documentation, but will not be detailed here, as this thesis only intends to overview the MDSplus system.

6.2.2. Parent/child

Below the top level of each shot are the nodes that point to data contained within the tree, or to other nodes. These nodes may be thought of as parents and children, following the hierarchical model. The *TOP* node is the parent of all other nodes in the tree. Parents and children both reside below *TOP*, the difference being parents cannot store data, but are meant only as hierarchical entities. Children are more versatile, in that they can be endpoints of the tree, where data is stored, or they can be parents themselves. Whether a node is considered a child or parent is relative to the reference point in the tree. In Figure 6.2, *TOP* is the parent of all other nodes, and *CHAMBER* is a child of *TOP*. However, it can also be said that *CHAMBER* is a parent of *CURRENT*, thus *CHAMBER* may be considered both a parent and a child. One of the endpoints of this *CHAMBER* subtree is *BDOT_VOLTAGE*, which contains signal data, and has no children. Thus, it is evident that a node can either have children of its own, or point to data. All nodes have metadata associated with them; however, this is not considered true data, but rather part of the data structure.

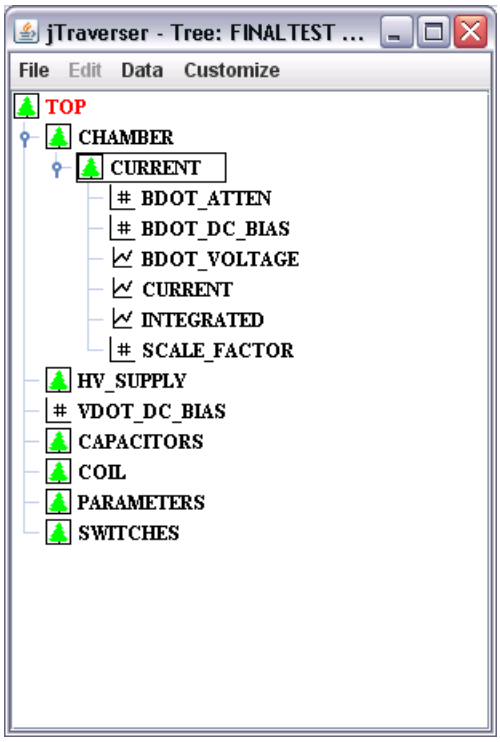

Figure 6.2: Example of an MDSplus tree layout.

6.2.3. Node names

To each node, a unique name is given that provides a unique trait that distinguishes it from all other nodes in the tree. In MDSplus, this name is known as its absolute reference, or full path name, and is constructed from the names of its parent nodes and the name of the node of interest. The naming convention gives our example node *BDOT_VOLTAGE* the absolute reference:

*\DATATREE::TOP*CHAMBER*CURRENT*BDOT_VOLTAGE* ,

where * denotes either a colon or a period, which is chosen automatically by MDSplus. If all node names are available, the tree structure may be uniquely determined. Later, we will see that this capability can be utilized to display the tree structure in Labview.

6.3. Node Metadata

To aid the explanation of the interfacing of MDSplus and Labview in the MegaGauss archiving program, we will feature the metadata aspects that this program uses most often. This metadata is typically queried by means of MDSplus' *getnci* method, which acquires node characteristic information specified by the method arguments.

6.3.1. ID Number (NID)

Just as each node has a unique absolute reference associated with it, each node also has a unique node identification (NID) number that can be queried. NIDs are useful for passing a node reference in a program, since a node can be more easily referenced with an integer rather than a character array containing the node's absolute reference. Sorting the nodes by NID results in a sorting of the nodes alphabetically (by absolute reference), then hierarchically. This makes it possible to prepare a pseudo-sorted array of absolute references, which can then be parsed to reconstruct the tree structure. This convenient pre-sorting prevents the tree reconstruction algorithm from having to look through the tree randomly to find the children and parents of each node.

6.3.2. Data Type

Every time a data node (also interpreted as an endpoint of a subtree) is declared during creation of the tree template, a data type (MDSplus calls this its usage) must be assigned to it. When this happens, the metadata is updated to make that assignment available for query. When the data node is later called by a program, the program does not need to know the data type to expect from the data node. Rather, it can query the data type of that node and adjust its processing of the data accordingly. The data types commonly used in MegaGauss are numbers (floating point and integers), character arrays

(strings), and *SIGNALS*. A *SIGNAL* is a special data type associated with MDSplus which is especially useful for time-resolved data, and is essentially a linked vector. One vector contains time steps, while another vector of the same length contains a value corresponding to an element in the time vector. That is, there are two vectors in parallel (e.g. time and voltage) that are stored as one unit of data. This prevents the user from being concerned with matching time steps with measured quantities, since these two are packaged as one unit.

6.3.3. Other Metadata

Several other metadata are available, such as node depth, name, and full path. Depth is used to determine how deeply a node resides in the layers of the tree (i.e. how many parents it has). This can be used to indicate how many parent nodes to search for when reconstructing a node's hierarchy. Name is simply the name of the node alone, which is useful when searching through a tree for a specific node whose hierarchy is not known, or for display purposes in a user interface. Full path is the absolute reference of a node. Although the full path, by definition, contains the node depth and name, it is often easier to use the NID of a node and query whatever data is desired, rather than parsing the absolute reference. Several other metadata are available in MDSplus, but the reader should refer to the MDSplus online documentation for further elaboration. (6)

Chapter 7: Writing MDSplus Trees via Labview

MegaGauss's main control program was originally written by staff at Sandia National Laboratories in the Labview (National Instruments, or NI) programming language. With its graphical, block diagram approach to coding, Labview is an intuitive development environment that allows programmers to implement algorithms rapidly, with reduced concern for syntax (versus C++, MATLAB, etc.). Also, Labview is designed to be compatible with NI's high-quality data acquisition products, such as those for MegaGauss instrumentation. For these reasons, the MegaGauss control program is implemented with Labview. To interface the MDSplus architecture with Labview, a specialized Labview program (virtual instrument, or VI), has been developed. Already provided are the mdscwrap methods described in Chapter 6; this novel program calls these mdscwrap methods to access the MDSplus tree. In doing so, it combines prepackaged Labview VIs and mdscwrap VIs to execute an algorithm that writes shot data to the tree (Fig. 7.1).

It should also be mentioned that Labview includes a tree structure of its own named TDM (8), which was initially examined as a possibility for this archive. However, due primarily to limitations in tree depth, and lack of versatility in data format, MDSplus was determined to be a more suitable fit. Since TDM is embedded in the Labview library, it is not readily apparent that TDM can be modified into a useful form for MegaGauss. In contrast, the software included in the MDSplus and mdscwrap distributions allow great freedom in tree structure and node format. Since these tools were already well defined and freely available, the decision to use MDSplus and mdscwrap was confirmed.

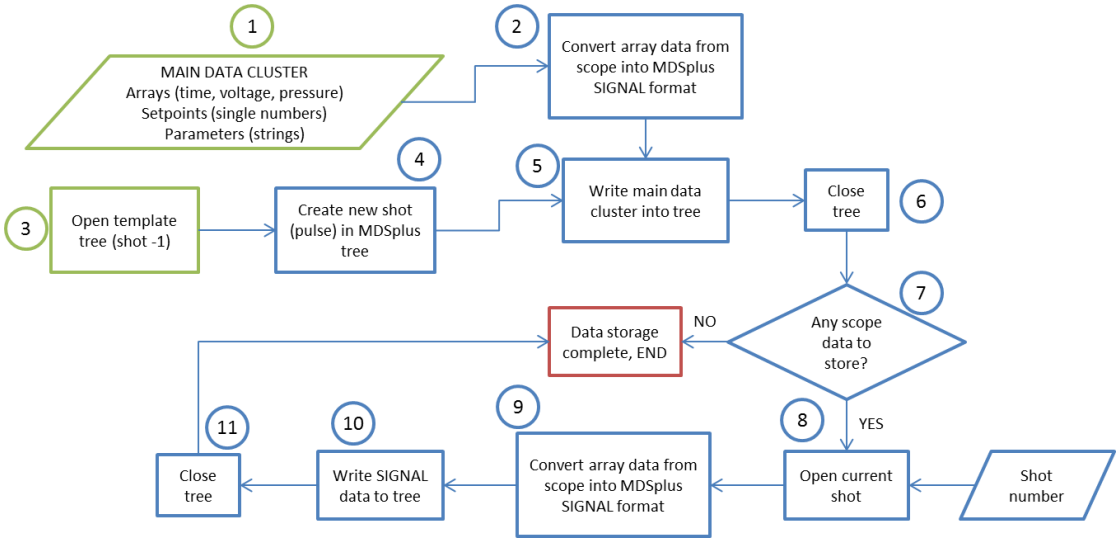

Figure 7.1: Flowchart schematic of data storage process. Steps are numbered for later reference.

7.1. USE OF MDSCWRAP IN LABVIEW

A specialized library of VIs, written for Labview 8.0 by a team at UW-Madison for their Pegasus Toroidal Experiment is used to interface Labview with the older MDSplus code. The naming of the methods in the mdscwrap library are quite self-explanatory, such as *getString.vi*, *putSignal.vi*, etc. All mdscwrap VIs accept Labview data objects as input, and output Labview data objects, but they also execute commands that are not carried out by Labview. Rather, the mdscwrap library calls the methods of the MDSplus library via a Labview code interface node (CIN), which carries out some specific C language routine. Labview data objects are fed into the CIN, where they are treated as parameters in a C function. When this function executes, it interacts with the MDSplus software through the C interface provided by MDSplus. Once this action is complete, the values returned by the function are converted into Labview objects by the CIN, and are available for use by the VI. The mdscwrap VIs follow this structure; at the heart of each VI is a CIN which executes the command associated with that VI (Fig. 7.2).

The *Expr* control serves as the parameter of the CIN, which outputs the value(s) associated with whatever *Expr*, usually an absolute reference, refers to.

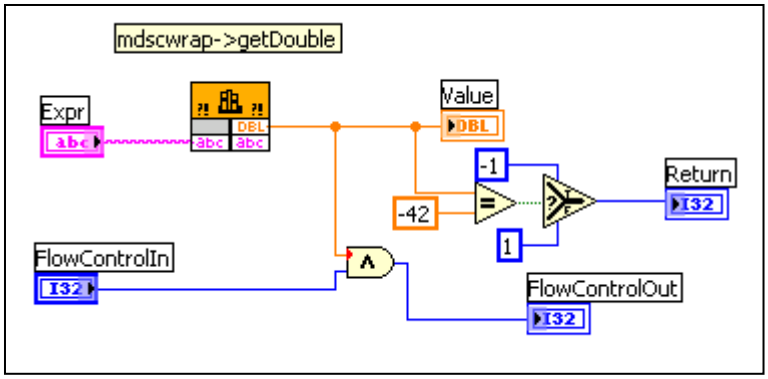

Figure 7.2: Labview block diagram for mdscwrap's *getDouble.vi*. A Labview code interface node (large block at top left) executes the relevant MDSplus commands to recover a double from the location referred to by *Expr*.

In the implementation of the data writer and reader programs, several of these mdscwrap VIs are called upon to create, modify, or read trees in the MegaGauss archive.

7.2. Writing Main Data Cluster to Tree[3]

Each shot in MegaGauss has a main data cluster associated with it. Some of the data in this cluster, a Labview data structure capable of containing different data types, is determined before the shot is initialized, such as shot description. Other data is real-time, such as the charge voltage on the capacitors. After a shot is fired, a dump relay is engaged to prevent accidental recharging of the capacitors; at this point, the shot may be considered complete. When this event occurs, the main control program triggers a

[3] This process corresponds to steps 1 – 6 of the flowchart in Fig. 7.1. An image of the entire block diagram is shown in Appendix D.

subroutine that sends the main data cluster into the tree creation VI, named *finaltestFrontPanelMDSplus.vi* (Fig 7.3).

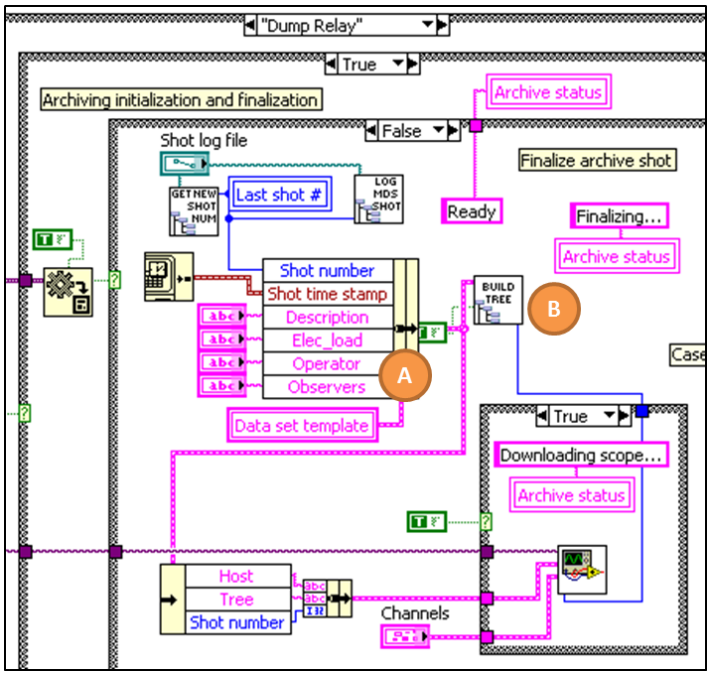

Figure 7.3: Portion of main control program (*MGP GUI new.vi*) that sends main data cluster (A) to archive subroutine (B) after dump relay is engaged.

Within this tree creation VI (Figs. 7.4-6, Appx. D), the template tree (shot -1) is opened (A), and a new shot is constructed based off of that template (B). MDSplus refers to this operation of creating a new shot as a pulse. After this completes, the newly created shot is opened (C), and the main data cluster is separated into its components (D), each of which is input into the tree according to the mdscwrap method that corresponds with its data type (E). Once all data is placed into the tree, the tree shot that was created is closed (F), and the new shot becomes a permanent part of the tree archive. In the referenced figures, nearly all subVIs in the block diagram are mdscwrap VIs.

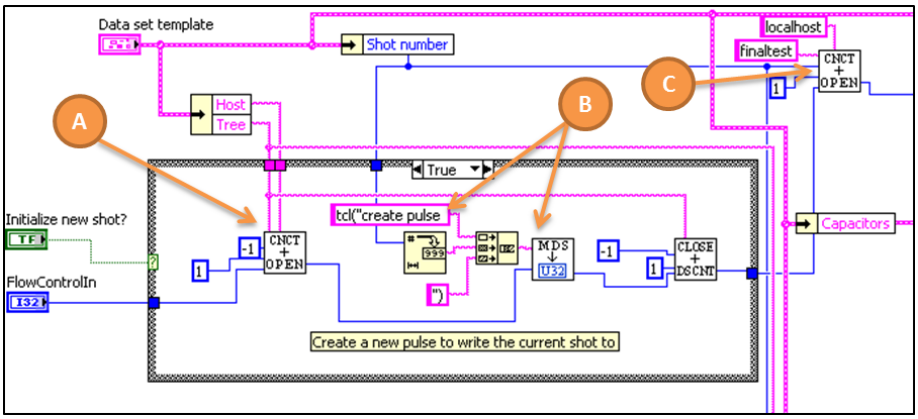

Figure 7.4: Creation and opening of new shot within tree *finaltest*. *CNCT + OPEN* is an example of an mdscwrap VI.

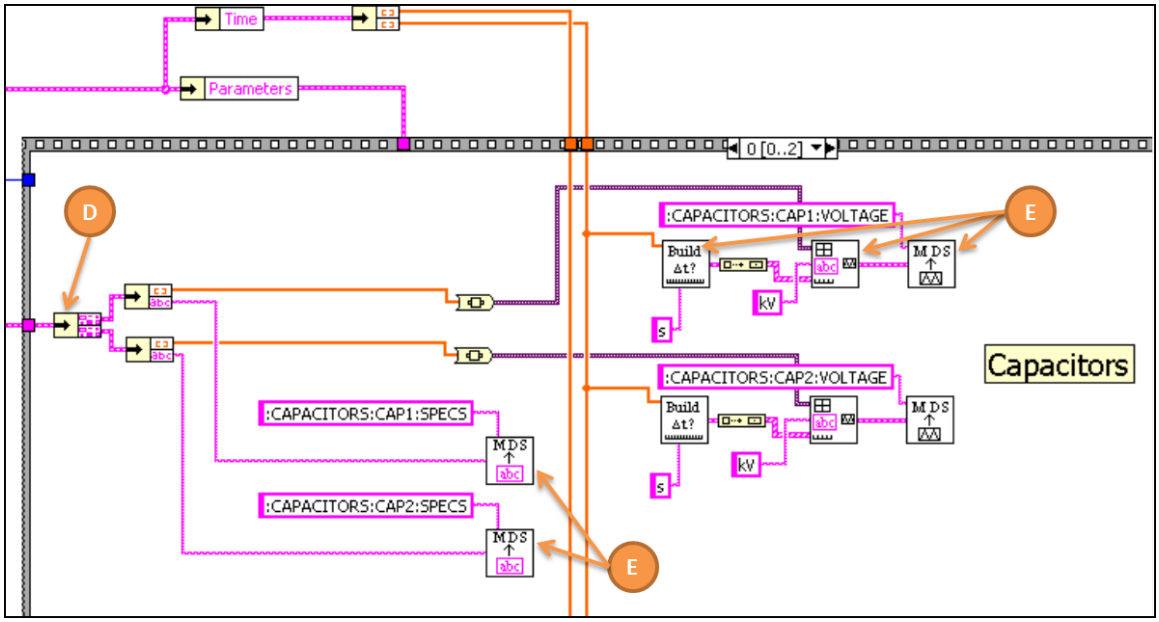

Figure 7.5: Cluster of capacitor-related data is unpacked and stored in the tree. Top right, arrays of voltage and time are conditioned to be stored as MDSplus signals, then sent to the tree. Bottom, capacitor specs in text string form are stored.

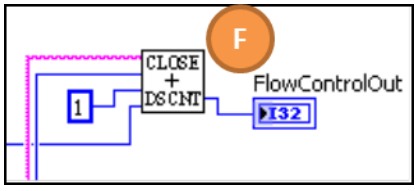

Figure 7.6: Process completes with order to close and disconnect from the MDSplus tree.

7.3. WRITING OSCILLOSCOPE DATA TO TREE[4]

In addition to the main data cluster, oscilloscope traces (e.g. B-dot current measurements) are usually available for storage into the tree. Using specialized Labview VIs that interface with Tektronix TDS 3000 series oscilloscopes (9), the traces are extracted and take the form of arrays of doubles (numeric format). One array, universal to all channels collected from the oscilloscope, is a time step array. The other arrays, up to four more, contain the signal amplitude in volts. By placing the desired channel's signal array alongside the time step array, the oscilloscope trace may be duplicated in Labview. This is exactly the technique used when bundling oscilloscope data to be stored into the tree.

When the MegaGauss system arrived from Sandia National Laboratories, the original programmers had written a routine (*Tek scope read1.vi*) to download oscilloscope information. To send this data into the MDSplus archive, an additional VI was necessary. This VI, named *TekscopeToTree.vi*, provides this functionality, and is embedded in the original oscilloscope VI provided by Sandia (Fig 7.7). When *TekscopeToTree.*vi is called, simple indexing operations and several mdscwrap VIs package the data into a form that can be placed into the tree archive (Fig 7.8).

[4] This process corresponds to steps 7 – 11 of the flowchart in Fig. 7.1.

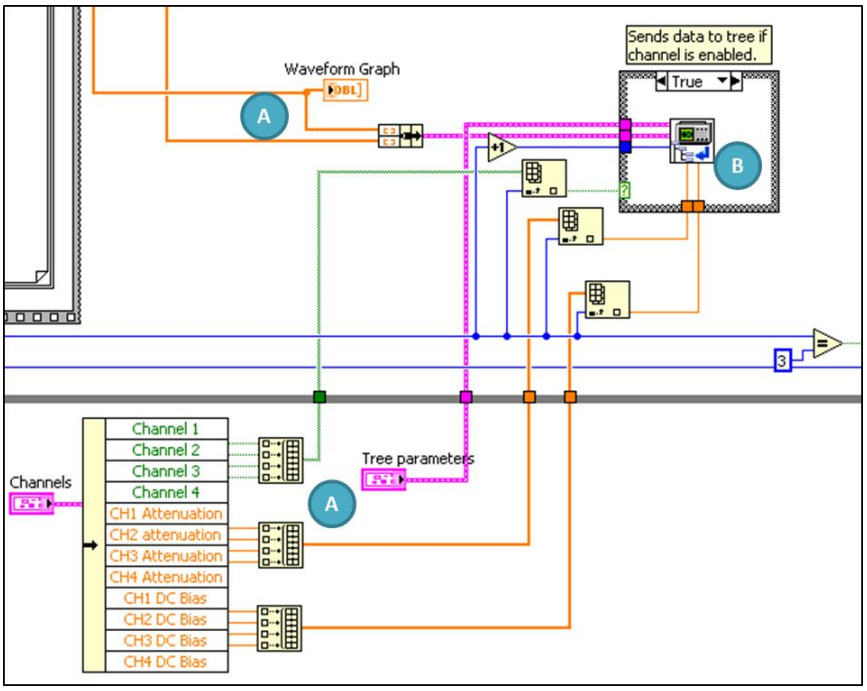

Figure 7.7: Positioning of *TekscopeToTree.vi* within *Tek scope read1.vi*. Relevant data is packaged (A) and sent to *TekscopeToTree.vi* (B) for archiving.

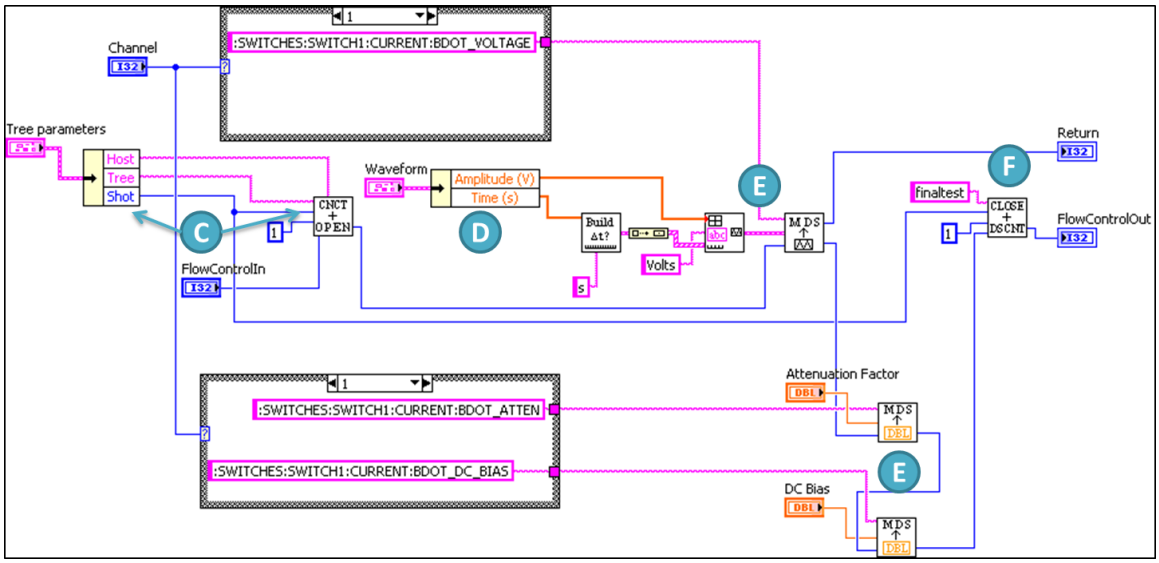

Figure 7.8: Block diagram of *TekscopeToTree.vi*. Tree parameters indicate tree and shot to open (C), then waveform (D) is converted into MDSplus *SIGNAL* format and archived, along with supporting data (E). Lastly, archive is closed (F).

Chapter 8: Reading MDSplus Trees via Labview

Although MDSplus is a suitable archive architecture, the previous chapter clearly showed that augmentation (i.e. mdscwrap VIs) of the default MDSplus interface is necessary to facilitate a simpler programming style when constructing a tree writing program. In the case of reading these trees, the situation is nearly identical. Although the standard MDSplus package includes several tools for visualizing a tree's hierarchy, structure, and data, these tools are obsolete when compared with the more advanced capabilities of a Labview program, especially in terms of the user interface. First, these MDSplus tools only provide basic functionality: viewing tree structure, simple plots of *SIGNAL*-type data, etc. Secondly, these tools are not integrable into Labview, and as such do not meet the objective to integrate control and data programs in Labview. A tree reading program, written in Labview, is thus necessary, but should not sacrifice the advantages given by the MDSplus architecture (e.g. hierarchy, adaptability).

Success in this programming objective comprises several requirements. First, the program must be able to extract the hierarchy data from the tree, and must be able to display that tree, preferably in its hierarchical form. Alternatively, all nodes could be listed, allowing the user to select from among them; however, this sacrifices the helpful branching visualization associated with tree data structures. Secondly, the program should be able to detect the data type contained in each data node, and should adapt its interpretation process accordingly. This is the programming concept of polymorphism: one program or function has several definitions, and automatically chooses which to use based on input.

Third, there must be a reasonably simple graphical user interface (GUI) which allows the user to work with data quickly, and without knowledge of the program's

underlying structure. This streamlined GUI will maximize user productivity by expediting data selection, visualization, and analysis. With the vast amount of data that MegaGauss is expected to acquire over its lifetime, this feature is crucial. Finally, and just as crucial, the program must perform simple analysis operations to facilitate quick data quantification. More difficult mathematical operations may be better performed with other software, necessitating a data exportation option.

Figure 8.1: Front panel of tree reading program (*traverseTreeMultiplot.VI*).

8.1. Tree Hierarchy Extraction

Extraction of tree structure is accomplished by searching the absolute paths for a predefined string. As explained previously (§6.2.3), every node contains its entire hierarchy within its absolute path. By supposing a node to be a parent, and examining the

names of all nodes one or more levels below the supposed parent, the children of this parent node can be located. Repeating this process for all nodes eventually extracts all parent/child relations, providing the necessary data for visually reconstructing the tree. This visual reconstruction is implemented via Labview's tree object, and is controlled by invoke node blocks; both tools are prepackaged with Labview. For all data sets acquired to date, this incremental parsing operation takes approximately five seconds to complete. An algorithm flowchart and the relevant portion of the Labview block diagram are illustrated in the following diagrams (Figs. 8.2-3).

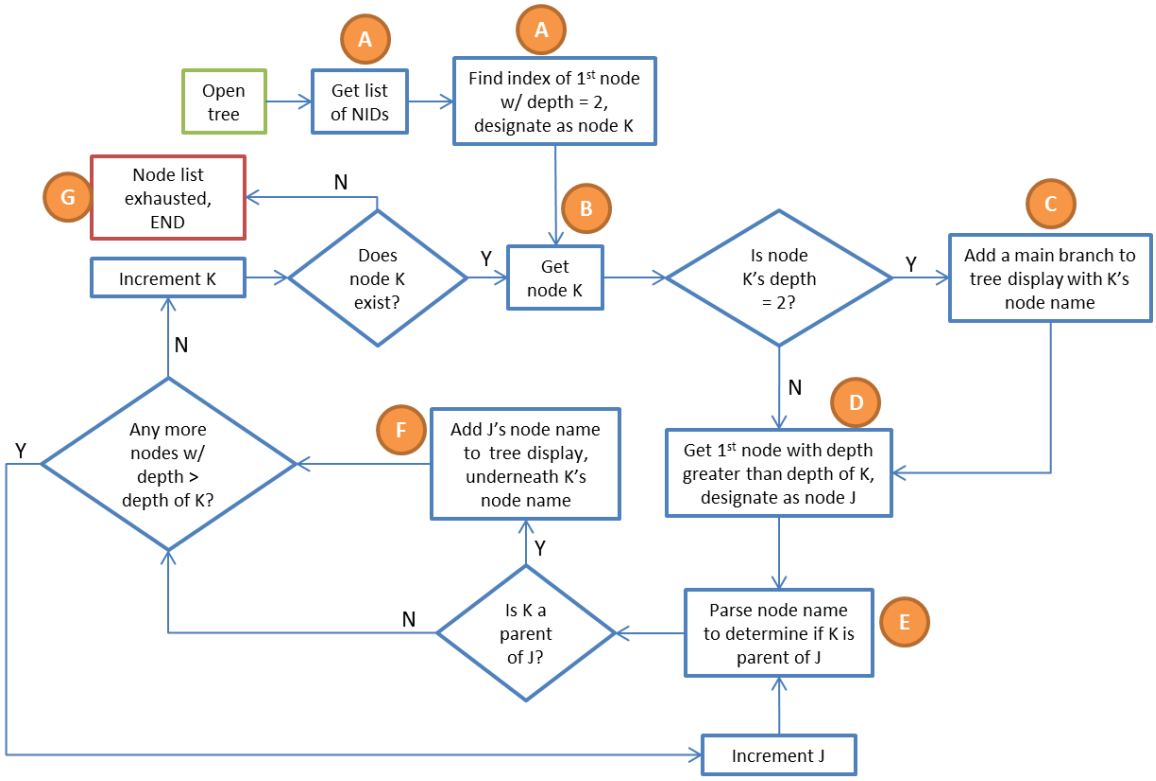

Figure 8.2: Algorithm for extracting tree hierarchy from node names.

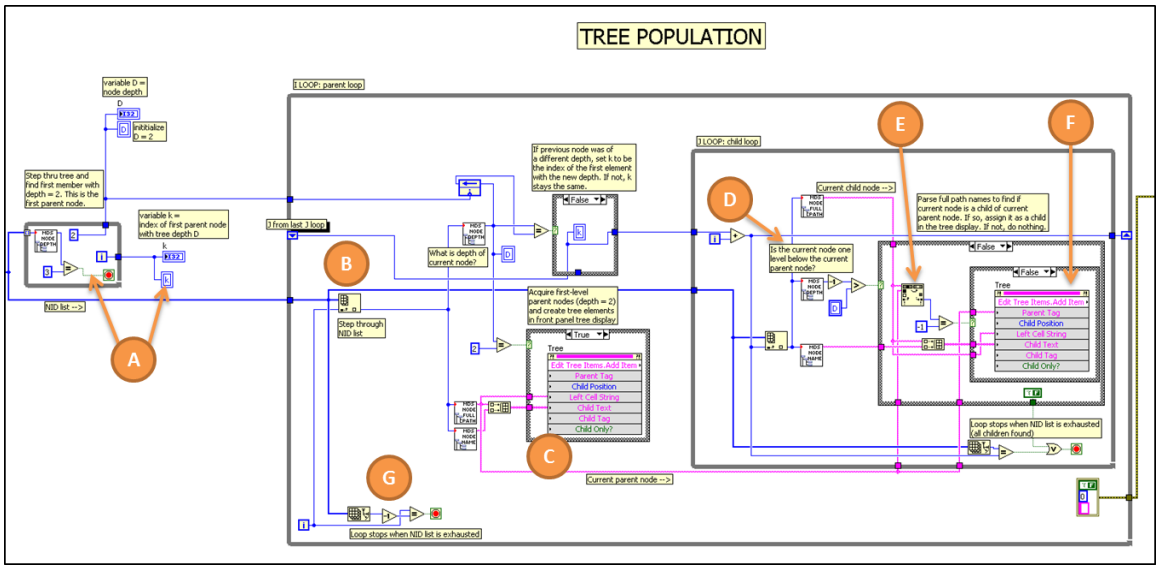

Figure 8.3: Block diagram implementation in Labview of tree hierarchy algorithm (Fig. 8.2).

8.2. POLYMORHPISM

Approaching the polymorphism problem is relatively simple, thanks to MDSplus's usage metadata. A *getnci* command (§6.3) is issued to an mdscwrap VI, which returns a number whose value is determined by the data type of the node of interest. This node is specified with its absolute path, which is linked to the currently selected item in the tree object on the front panel. The number indicating usage, once returned from the mdscwrap VI, controls a case structure which appropriately conditions the data extracted from the node. The simple algorithm and code is shown below (Figs. 8.4-5).

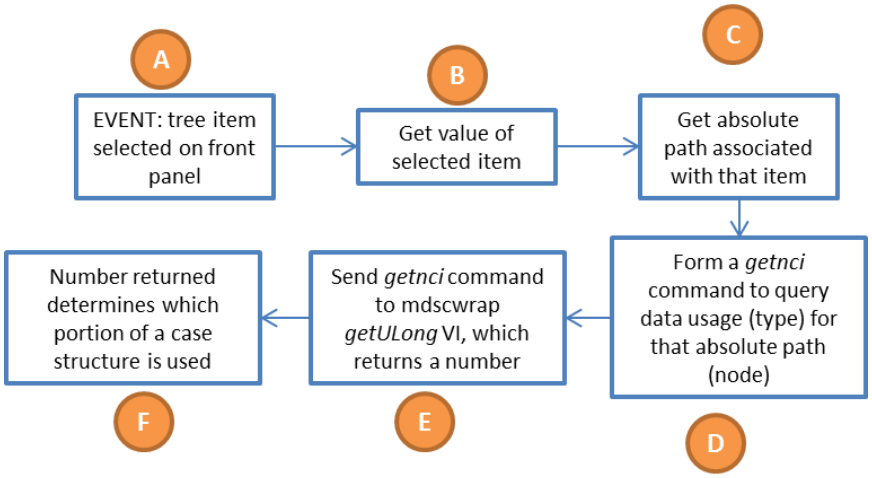

Figure 8.4: Algorithm for querying data type when an item on the front panel tree object is selected.

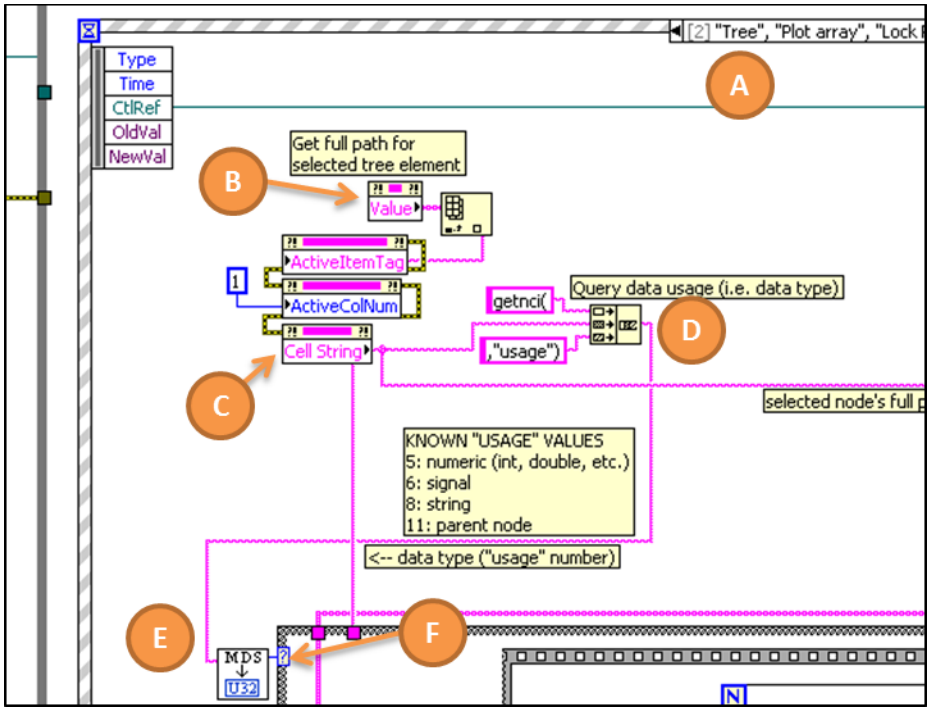

Figure 8.5: Block diagram implementation of node usage algorithm (Fig. 8.3) in Labview.

8.3. GUI CONSIDERATIONS[5]

To streamline operation of the GUI, the reader program is designed with a front panel that adapts to the data type being selected. For example, when the user selects a node that contains string-type data, the GUI automatically hides the display for the previous data type (assuming it was not another string), and displays a text box containing the string. A similar display change occurs when numeric or *SIGNAL* data is chosen, preventing distractions from a cluttered interface.

Once the tree structure is extracted (§8.1), a tree front panel object is used to display the data. This object is clickable, and only shows the short names of the nodes rather than the absolute paths; these would be too long to interpret. Each item in such a tree object is multi-column, and this feature is used to link the short names with the absolute paths, although only the column with the short names is visible on the GUI. This approach allows the user to view the short names for readability, while the program can use the absolute path when performing operations on the selected item.

One of the most important features of the GUI is the *SIGNAL* plotting window. This uses the Labview XY plot object, and plots up to four data sets on a time scale, effectively duplicating the oscilloscope trace. In the program, each plot and its associated data includes raw data (amplitude and time), parameters that control the plot's display, and statistics of the plot data. Programmatically, these are bundled into a cluster object in the block diagram which is linked to the front panel controls and indicators, allowing the user to manipulate these parameters and view the statistics.

[5] Refer to Figure 8.1 during this discussion.

8.4. ANALYSIS OPTIONS

When a *SIGNAL* node is selected, the display mode shows the plot, and simple statistics of what is being viewed. These statistics are the global maximum, minimum, and mean. Having this capability allows the user quick assessment of the peak of any plotted signal. For example, if the scaling factors for the plot are set correctly, this translates to the ability to view the peak current value in one click. Also included in the XY plot are two vertical position cursors, which function as time markers. These markers designate a region of interest (ROI) that has its own max/min/mean set, providing a way to analyze a local region of a plot.

The statistical mean of this (ROI) is especially useful, since, if the ROI is set to the time frame before the shot begins, it can be taken as the constant offset of the signal. Although the offset may appear insignificant, the algorithm that integrates the B-dot data is very sensitive to such an offset. Left unchecked, this offset will produce a slope in the integrated plot, providing a misleading integral that prevents the user from reading a meaningful peak value.

8.4.1. Data Plotting

The plot window is designed to plot up to four signals at once, providing the capability to compare Switch 1 and 2, for example. To allow the user to select which plot will change upon selection of a *SIGNAL* node in the tree display, a plot locking functionality is built into the program. Once a desired item is selected for plotting, the user can “lock” that plot, meaning that plot will remain linked to the last selected tree item. In this way, the user can move on to selecting the next plot upon which the first can be overlaid, without changing the first (locked) plot.

Adjustments to the data to compensate for attenuators, B-dot proportionality constants, etc. are allowed the user by means of a simple numeric scale factor. Each plot has a scale factor associated with it, and is part of the cluster associated with each plot. Raw amplitude data is multiplied by this factor and plotted. A similar correction factor is the bias correction value, termed the zero reference for the plot. As mention in the previous section, the ROI mean, if the ROI is the region before the shot begins, is the zero reference for that plot. A zero reference may be computed for any given time frame, of course, but this particular zero reference is necessary for conditioning the plot for integration.

A key feature of the plot window and its related controls is its integration capability. This uses the prepackaged Labview integration algorithm to compute and display the integral of the selected plot. To ensure accuracy, the zero reference of the plot must be obtained and applied by the user. This is a simple process: the user selects the appropriate ROI, sets the zero reference, and indicates the integrator should use that correcting offset during its computation. Before doing this, the scale factor should already be set to its final value, as changing the scale factor later will amplify the raw data (and thus the offset), preventing the zero reference correction from being effective.

8.4.2. Export to Clipboard

To allow the user the flexibility to export the plot data to another program, such as Excel, MATLAB, or Mathematica, the GUI has the ability to export a comma separated value (CSV) data set to the Clipboard. Doing this will allow the user to effectively copy and paste the data in the plot window. It should be noted that the data being copied is not raw data, but rather the data being plotted, meaning whatever conditioning has been implemented propagates through the copy-to-Clipboard operation. To copy the raw data,

the user must deactivate all signal conditioning (i.e. set all scale factors to zero, do not integrate, etc.).

Appendices

APPENDIX A: MEGAGAUSS CURRENT DRIVER CIRCUIT

A.1. Overall Circuit Schematic

NOTES: Charging and trigger circuitry not pictured. Except for switch can and load, values for circuit components are found in (5). Switch can and load inductances were computed by the author (Appxs. A.2-3).

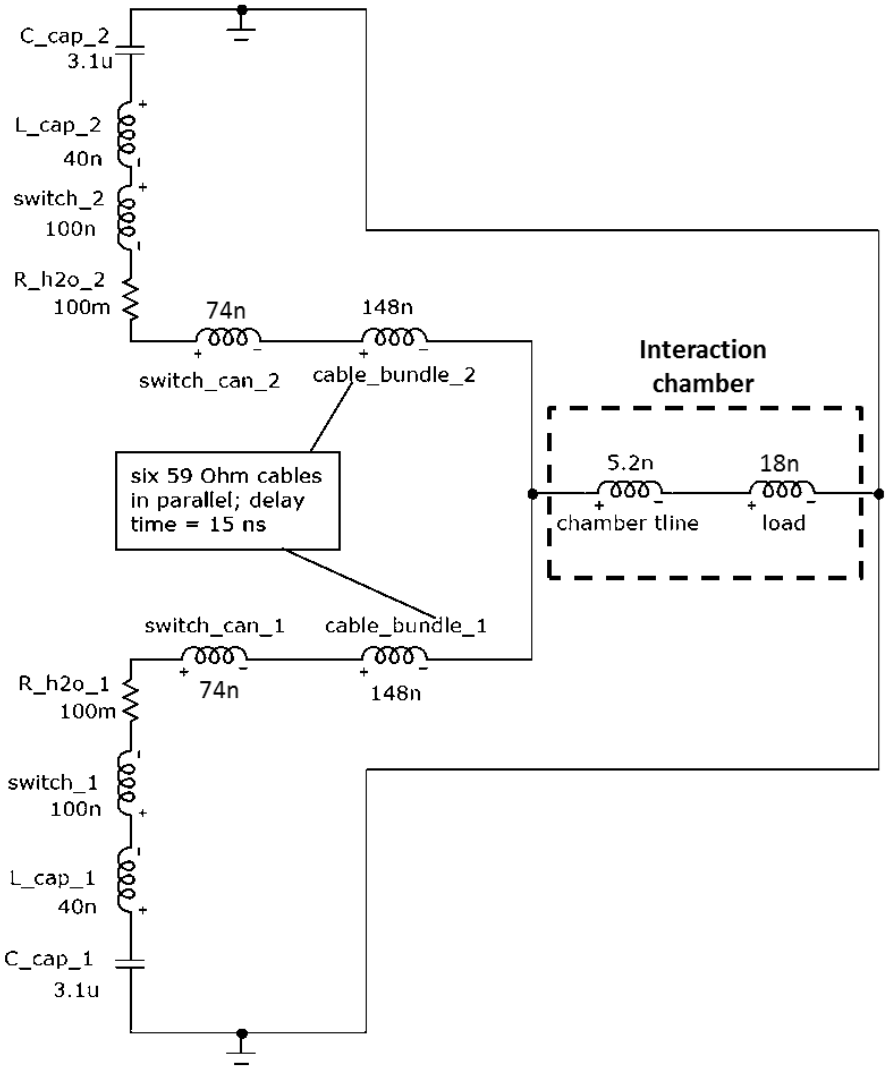

A.2. Computation of Switch Can Inductance.

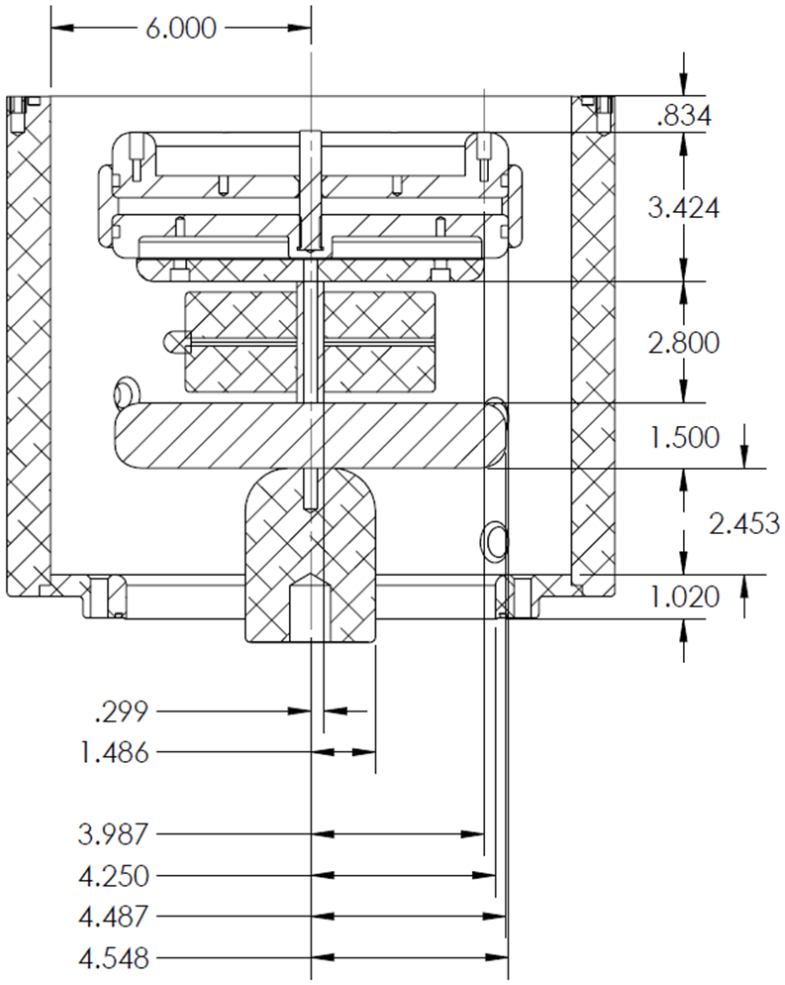

$$L_{coaxial} = \frac{\mu_0}{2\pi} \cdot \left[1.0 \cdot \ln\left(\frac{4.3}{1.5}\right) + 2.5 \cdot \ln\left(\frac{6}{1.5}\right) + 1.5 \cdot \ln\left(\frac{6}{4.5}\right) + 2.8 \cdot \ln\left(\frac{6}{.30}\right) + 3.4 \cdot \ln\left(\frac{6}{4.5}\right) + .83 \cdot \ln\left(\frac{6}{4.0}\right)\right] \quad \text{(A.1)}$$

$$= 74\ nH$$

A.3. Computation of ½ Inch ID Helmholtz Coil

The standard electrical load for the MegaGauss shots discussed in this thesis is a Helmholtz coil of radius ¼". Using the magnetic field equation for a Helmholtz coil, Faraday's Law, and the inductor/voltage relation, the inductance of such a load is estimated. Since the coil is clamped to the transmission line approximately where the circular (coil) region of the load starts, the inductance of the straight feeds do not carry current, and their inductance is irrelevant. Some small portion of the feeds is used to transport the current to the coil region, but this is ignored to simplify the calculation. It is also likely that the skin effect causes most current to flow on the ends of the coil, rather than the inner surfaces of the two loops of the Helmholtz coil. As such, this coil may be more like a solenoid than a Helmholtz. For comparison, the inductance of a solenoid will also be found, and compared with the Helmholtz inductance; it will become apparent that the total inductance of the MegaGauss circuit will not be significantly altered if the skin effect is ignored.

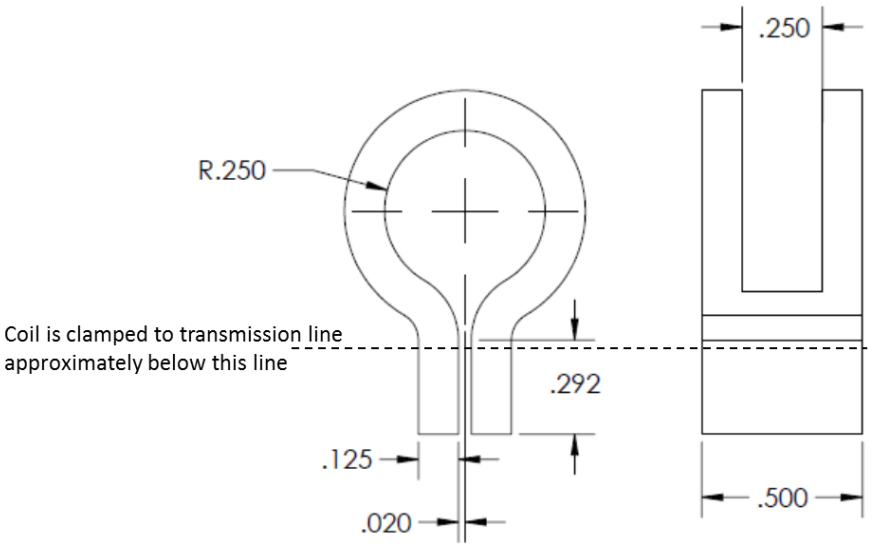

$$B_{Helmholtz} = \left(\frac{4}{5}\right)^{3/2} \frac{\mu_0 nI}{R} \tag{A.2}$$

$$L_{solenoid} = \frac{\mu_0 n^2 A}{l} = \frac{\mu_0 \pi (.25\ in)^2}{.50\ in} = 12.5\ nH \tag{A.3}$$

It should be noted that A.2 only applies at the center of the coil. This field will be assumed uniform throughout the coil's cross-section to simplify the calculation. Recall the procedure in Equation 2.3 for computing voltage across a B-dot gives:

$$E \cdot 2\pi a = S \cdot dB/dt, \tag{A.4}$$

and understand that voltage across the coil region of the load is expressed as the electric field around the inner perimeter of the coil:

$$v = E \cdot 2\pi a = S \cdot dB/dt \tag{A.5}$$

Combining these, using the expression for magnetic field from the Helmholtz, we get:

$$L \cdot \partial I/\partial t = \pi R^2 \cdot \frac{d}{dt}\left[\left(\frac{4}{5}\right)^{3/2} \frac{\mu_0 nI}{R}\right]. \tag{A.4}$$

The current derivative disappears, leaving the expression for Helmholtz inductance:

$$L = 0.716\mu_0 \cdot \pi R \cdot n. \tag{A.4}$$

where R is the coil radius and n is the number of turns in each Helmholtz coil. For the dimensions of the coil used in MegaGauss, we get:

$$L = 0.716\mu_0 \cdot \pi \cdot (.25\ in) = 18\ nH. \tag{A.4}$$

APPENDIX B: CALIBRATION SPREADSHEETS FOR B-DOTS

B.1. B-dot Calibration Spreadsheet for Switch #1

B-dot attenuation factor:	2	
CVR attenuation factor:	1000	
CVR resistance:	0.004987	Ohms

Following are corrected values based on the raw data, adjusted by the parameters above

	Maximum	
Shot 13, B-dot max (integrated)	1.35	μV*s
Shot 13, CVR voltage	597	V
Shot 13, CVR current	119.71	kA
Shot 15, B-dot max (integrated)	1.34	μV*s
Shot 15, CVR voltage	605	V
Shot 15, CVR current	121.32	kA
Shot 16, B-dot max (integrated)	1.34	μV*s
Shot 16, CVR voltage	596	V
Shot 16, CVR current	119.51	kA
Shot 17, B-dot max (integrated)	1.34	μV*s
Shot 17, CVR voltage	598	V
Shot 17, CVR current	119.91	kA
Shot 18, B-dot max (integrated)	1.34	μV*s
Shot 18, CVR voltage	605	V
Shot 18, CVR current	121.32	kA

	Mean						
B-dot max (integrated)	1.3420	μV*s	**≈**	**1.34**	**±**	**0.004**	μV*s
CVR current	120.3529	kA	**≈**	**120**	**±**	**0.9**	kA
Switch 1 B-dot calibration:	89.6818	kA/(μV*s)	**≈**	**89.6**	**±**	**0.73**	kA/(μV*s)
				% error:	**±**	**1**	%
	Std. Dev.						
B-dot max (integrated)	0.00447	μV*s					
CVR current	0.89001	kA					

Conclusion: ***One microvolt-second (μV*s) on Switch 1's integrated B-dot signal indicates an output of 89.6 kA delivered to the load.***

B.2. B-dot Calibration Spreadsheet for Switch #1

B-dot attenuation factor:	2	
CVR attenuation factor:	1000	
CVR resistance:	0.004987	Ohms

Following are corrected values based on the raw data, adjusted by the parameters above

	Maximum	
Shot 68, B-dot max (integrated)	-1.65	µV*s
Shot 13, CVR voltage	602	V
Shot 13, CVR current	120.71	kA
Shot 69, B-dot max (integrated)	-1.65	µV*s
Shot 15, CVR voltage	610	V
Shot 15, CVR current	122.32	kA
Shot 70, B-dot max (integrated)	-1.66	µV*s
Shot 16, CVR voltage	599	V
Shot 16, CVR current	120.11	kA
Shot 71, B-dot max (integrated)	-1.66	µV*s
Shot 17, CVR voltage	600	V
Shot 17, CVR current	120.31	kA
Shot 72, B-dot max (integrated)	-1.65	µV*s
Shot 18, CVR voltage	600	V
Shot 18, CVR current	120.31	kA

	Mean						
B-dot max (integrated)	-1.6540	µV*s	**≈**	**-1.65**	**±**	**0.005**	µV*s
CVR current	120.7540	kA	**≈**	**121**	**±**	**0.9**	kA
Switch 1 B-dot calibration:	-73.0072	kA/(µV*s)	**≈**	**-73.3**	**±**	**-0.60**	kA/(µV*s)
				% error:	**±**	**1**	%
	Std. Dev.						
B-dot max (integrated)	0.00548	µV*s					
CVR current	0.90123	kA					

Conclusion: ***One (absolute value) microvolt-second (µV*s) on Switch 2's integrated B-dot signal indicates an output of 73.3 kA delivered to the load.***

APPENDIX C: RAW DATA FOR BACKGROUND PRESSURE TESTS.

Chamber background pressure (Torr)	Shot number(s)	Approximate time of breakdown $[\mu s]$ ($t_{peak} \approx 1.5\ \mu s$)	Breakdown after peak field?
5.20E-05	116	2.77	Yes
6.00E-05	110 , 111	3.52, 2.94	Yes (2x)
2.50E-02	76	0.24	No
2.60E-02	75	0.24	No
4.20E-02	77	0.18	No
6.00E-02	100	0.58	No
8.50E-02	78	< 0.10	No
1.01E-01	79	0.2	No
2.00E-01	104	0.17	No
2.02E-01	81	0.14	No
3.10E-01	80	< 0.10	No
4.05E-01	82	0.08	No
4.28E-01	105	0.15	No
5.10E-01	83	0.1	No
8.50E-01	103	0.11	No
3.32E+00	84	< 0.10	No
4.38E+00	102	0.1	No
9.90E+00	85	< 0.10	No
8.70E+01	97	0.13	No
2.85E+02	94, 95	0.27, 0.16	No
3.65E+02	98	0.17	No
5.20E+02	93	none	N/A
5.90E+02	99	none	N/A
7.60E+02	96	none	N/A

APPENDIX D: ENTIRE BLOCK DIAGRAM FOR *FINALTESTFRONTPANELMDSPLUS.VI*.

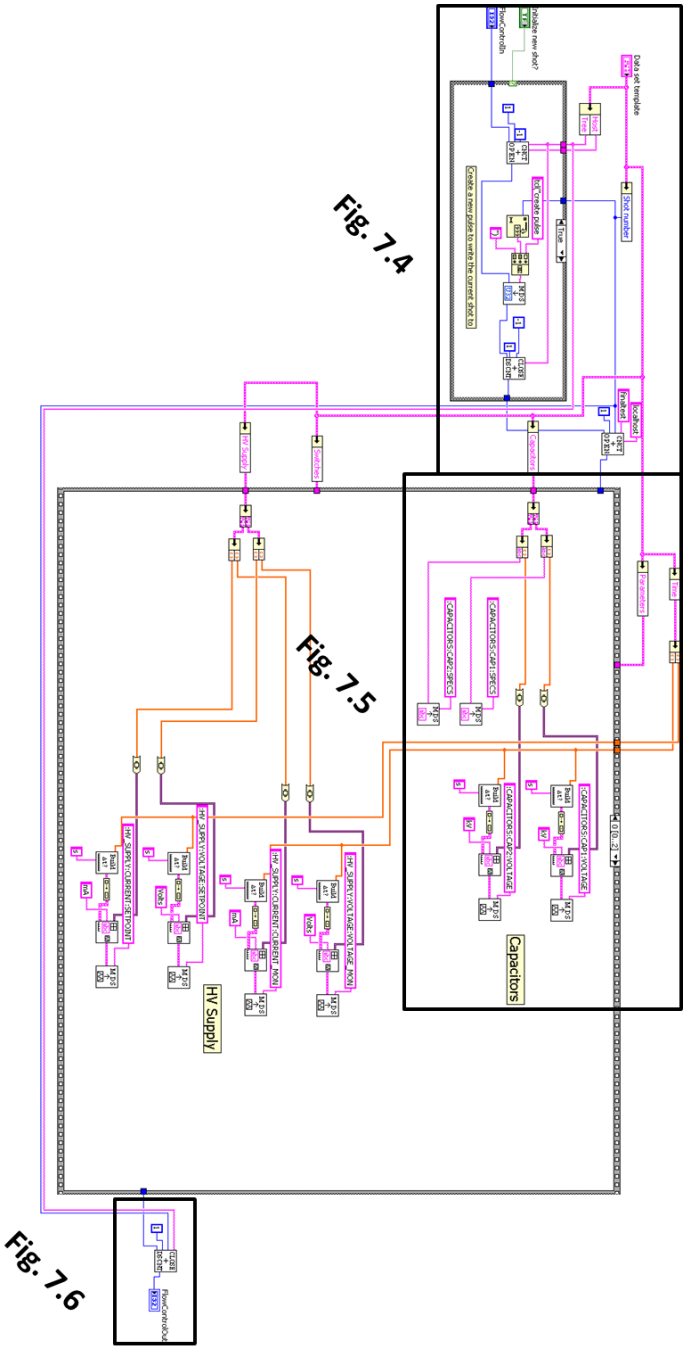

References

1. Ditmire, T., et al. Nuclear fusion from explosions of femtosecond laser-heated deuterium clusters. *Nature.* 1999, Vol. 398, 8 April.

2. K.W. Struve, J.L. Porter, D.C. Rovang. *Megagauss Field Generation for High-Energy-Density Plasma Science Experiments.* Albuquerque : Sandia National Laboratories, 2008.

3. Bluhm, Hansjoachim. *Pulsed Power Systems: Principles and Applications.* Berlin : Springer, 2006.

4. Hayt, William H., Jr, Kemmerly, Jack E. and Durbin, Steven M. *Engineering Circuit Analysis.* New York : McGraw-Hill, 2002. ISBN 0-07-112227-3.

5. *Recent Pulsed-Power Technology Advances In The Pulsed Power Sciences Center At Sandia National Laboratories.* K. W. Struve, et al. Geneva : IET European Pulsed Power Conference 2009, 2009.

6. London, Mark. Introduction - MdsWiki. *MDSplus web site.* [Online] [Cited: April 29, 2011.] http://www.mdsplus.org/index.php/Introduction.

7. Bongard, Michael. Pegasus Toroidal Experiment web site. *MDSplus software.* [Online] December 17, 2009. [Cited: April 29, 2011.] http://pegasus.ep.wisc.edu/Software/MDSplus.htm.

8. Introduction to LabVIEW TDM Streaming VIs - Developer Zone - National Instruments. *National Instruments web site.* [Online] [Cited: April 29, 2011.] http://zone.ni.com/devzone/cda/tut/p/id/3539.

9. National Instruments. Instrument Driver Network. *Tektronix Tektronix TDS 3000 Series Oscilloscope - Ethernet, IEEE 488.2 (GPIB), Serial Driver for LabVIEW - National Instruments.* [Online] [Cited: April 29, 2011.] http://sine.ni.com/apps/utf8/niid_web_display.download_page?p_id_guid=014E9F890ACE6DA0E0440003BA7CCD71.

10. Personal email communication with Barth Electronics sales representative, Doug Sokoll. April 29, 2011.